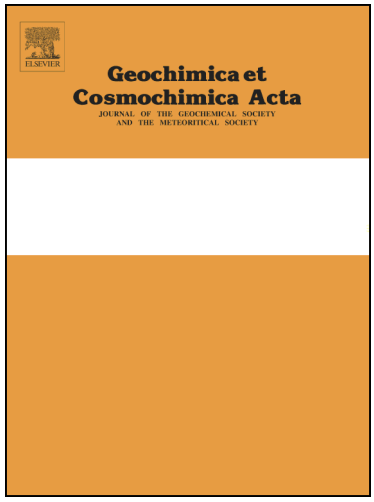

Copper-arsenic decoupling in an active geothermal system: a link between pyrite and fluid composition

Daniele Tardani, Martin Reich, Artur P. Deditius, Stephen Chryssoulis, Pablo Sánchez-Alfaro, Jackie Wrage, Malcolm P. Roberts

PII: S0016-7037(17)30058-3
DOI: http://dx.doi.org/10.1016/j.gca.2017.01.044
Reference: GCA 10138

To appear in: *Geochimica et Cosmochimica Acta*

Received Date: 30 June 2016
Revised Date: 23 January 2017
Accepted Date: 25 January 2017

Please cite this article as: Tardani, D., Reich, M., Deditius, A.P., Chryssoulis, S., Sánchez-Alfaro, P., Wrage, J., Roberts, M.P., Copper-arsenic decoupling in an active geothermal system: a link between pyrite and fluid composition, *Geochimica et Cosmochimica Acta* (2017), doi: http://dx.doi.org/10.1016/j.gca.2017.01.044

Final (revised) version submitted to Geochimica *et* Cosmochimica Acta

Copper-arsenic decoupling in an active geothermal system: a link between pyrite and fluid composition

Daniele TARDANI[1,2*], Martin REICH[1,2], Artur P. DEDITIUS[3], Stephen CHRYSSOULIS[4], Pablo SÁNCHEZ-ALFARO[1,2], Jackie WRAGE[1,2], Malcolm P. ROBERTS[5]

[1] Department of Geology, FCFM, Universidad de Chile, Santiago 8370450, Chile

[2] Andean Geothermal Center of Excellence (CEGA), FCFM, Universidad de Chile, Santiago 8370450, Chile

[3] School of Engineering and Information Technology, Murdoch University, Western Australia 6150, Australia

[4] Advanced Mineral Technology Laboratory (AMTEL), London, Ontario N6G 4X8, Canada

[5] Center for Microscopy, Characterisation and Analysis (CMCA), University of Western Australia, Crawley, 6009, WA, Australia

* E-mail: daniele.tardani@ing.uchile.cl

Keywords: trace elements, pyrite, Cu-As decoupling, Tolhuaca Geothermal System, Southern Volcanic Zone

Abstract

Over the past few decades several studies have reported that pyrite hosts appreciable amounts of trace elements which commonly occur forming complex zoning patterns within a single mineral grain. These chemical zonations in pyrite have been recognized in a variety of hydrothermal ore deposit types (e.g., porphyry Cu-Mo-Au, epithermal Au deposits, iron oxide–copper–gold, Carlin-type and Archean lode Au deposits, among others), showing, in some cases, marked oscillatory alternation of metals and metalloids in pyrite growth zones (e.g., of Cu-rich, As-(Au, Ag)-depleted zones and As-(Au, Ag)-rich, Cu-depleted zones). This decoupled geochemical behavior of Cu and As has been interpreted as a result of chemical changes in ore-forming fluids, although direct evidence connecting fluctuations in hydrothermal fluid composition with metal partitioning into pyrite growth zones is still lacking. In this study, we report a comprehensive trace element database of pyrite from the Tolhuaca Geothermal System (TGS) in southern Chile, a young and active hydrothermal system where fewer pyrite growth rims and mineralization events are present and the reservoir fluid (i.e. ore-forming fluid) is accessible. We combined the high-spatial resolution and X-ray mapping capabilities of electron microprobe analysis (EMPA) with low detection limits and depth-profiling capacity of secondary-ion mass spectrometry (SIMS) in a suite of pyrite samples retrieved from a ~1 km drill hole that crosses the argillic (20 to 450 m) and propylitic (650 to 1000 m) alteration zones of the geothermal system. We show that the concentrations of precious metals (e.g., Au, Ag), metalloids (e.g., As, Sb, Se, Te), and base and heavy metals (e.g., Cu, Co, Ni, Pb) in pyrite at the TGS are significant. Among the elements analyzed, As and Cu are the most abundant with concentrations that vary from sub-ppm levels to a few wt. % (i.e., up to ~5 wt. % As, ~1.5 wt. % Cu). Detailed wavelength-dispersive spectrometry (WDS) X-ray maps and SIMS depth vs. isotope concentration profiles reveal that pyrites from the TGS are characterized by chemical zoning where the studied elements occur in different mineralogical forms. Arsenic and Co occur as structurally bound elements in pyrite, Cu and Au in pyrite can occur as both solid solution and submicron-sized particles of chalcopyrite and native Au (or Au tellurides), respectively. Pyrites from the deeper propylitic zone do not show significant zonation and high Cu-(Co)-As concentrations correlate with each other. In contrast, well-developed zonations were detected in pyrite from the shallow argillic alteration zone, where Cu(Co)-rich, As-depleted cores alternate with Cu(Co)-depleted, As-rich rims. These microanalytical data were contrasted with chemical data of fluid

inclusions in quartz and calcite veins (high Cu/As ratios) and borehole fluid (low Cu/As ratios) reported at the TGS, showing a clear correspondence between Cu and As concentrations in pyrite-forming fluids and chemical zonation in pyrite. These observations provide direct evidence supporting the selective partitioning of metals into pyrite as a result of changes in ore-forming fluid composition, most likely due to separation of a single-phase fluid into a low-density vapor and a denser brine, capable of fractionating Cu and As.

1. INTRODUCTION

Sulfide minerals are common in many active geothermal systems worldwide, including the Salton Sea in California (Skinner et al., 1967; McKibben and Elders, 1985; McKibben et al., 1988a, b; Hulen et al., 2004), Rotokawa, Ngawha and Broadlands-Ohaaki in New Zealand (Krupp and Seward, 1987; Cox and Browne, 1995; Simmons and Browne, 2000), Kirishima and Yanaizu-Nishiyama in Japan (Shoji et al., 1989; 1999), Mataloko in Indonesia (Koseki and Kazuo, 2006; Koseki and Nakashima, 2006), Joaquina in Guatemala (Libbey et al., 2015) and Reykjanes in Iceland (Libbey and William Jones, 2016). Among sulfides, pyrite is ubiquitous in geothermal systems although most studies have focused on their metal-rich fossil counterparts (i.e., ore deposits). Mineral chemistry studies of pyrite in hydrothermal ore deposits, including Carlin-type and Archean lode Au deposits, porphyry Cu deposits, epithermal Au-Ag deposits and iron oxide–copper–gold deposits (IOCG), among others, have pointed out that this sulfide is a major host of metals and metalloids such as Au, Ag, Cu, Pb, Zn, Co, Ni, As, Sb, Se, Te, Hg, Tl, and Bi (Cook and Chryssoulis, 1990; Fleet et al., 1993; Huston et al., 1995; Simon et al., 1999; Large et al., 2009; Palenik et al., 2004; Vaughan and Kyin, 2004; Reich et al., 2005; 2006; Barker et al., 2009; Cook et al., 2009; Deditius et al., 2009a,b; 2011; 2014; Sung et al., 2009; Koglin et al., 2010; Ulrich et al., 2011; Peterson and Mavrogenes, 2014; Steadman et al., 2015; Gregory et al., 2016; Reich et al., 2016; Tanner et al., 2016). These studies have also provided analytical and spectroscopic evidence showing that the incorporation and micro-textural distribution of these elements is complex in pyrite, occurring in both solid solution and/or as metal nanoparticles or nano-inclusions forming chemically-heterogeneous growth and sector zones. This variation in the chemical composition of pyrite has been used to elucidate the chemical evolution of hydrothermal systems and ore deposits at various scales (Muntean et al. 2011), and has also been evaluated as a vectoring tool in mineral

exploration (Baker et al., 2006; Belousov et al., 2014; Franchini et al., 2015; Gregory et al., 2016; Soltani Dehnavi et al., 2015). More recently, trace element contents in marine sulfides, particularly pyrite, are being used to answer some fundamental questions about the evolution of the Earth's ocean-atmosphere system, including how nutrient trace element cycles relate to geodynamic cycles, biological evolution and mass extinction events (Large et al., 2014; 2015a, b; Gregory et al., 2015a, b; Long et al., 2015).

Recent studies have reported complex oscillatory growth and sector zoning in pyrite from hydrothermal ore deposits where elements such Cu, Au and As are preferentially enriched and show a decoupled geochemical behavior (Deditius et al., 2008; 2009; 2011; Reich et al., 2013). Arsenic-rich zones containing Au, Ag, Sb, Te, and Pb, can alternate with Cu-rich zones with significantly lower concentrations of these elements, and barren pyrite zones with no other elements. These chemical zoning features have been related to selective partitioning of metals into pyrite as the result of physico-chemical changes in the ore-forming fluids (Deditius et al., 2009; Peterson and Mavrogenes, 2014; Reich et al., 2013; 2016). Furthermore, in low-temperature sedimentary environments, recent studies have shown that diagenetic pyrite formed within the anoxic sediments can record the composition of pore water (Berner et al., 2006; 2013; Gregory et al., 2014).

In particular, the presence of finely spaced multiple growth zones in pyrite where Cu and As are geochemically decoupled provide evidence that the composition of shallow hydrothermal systems can be affected intermittently and repetitively by vapors, probably from underlying magmas (Deditius et al., 2009; Reich et al., 2013). However, direct observations linking the alternating metal concentrations in pyrite zonations and the chemical evolution of the ore-forming fluid are still lacking. Furthermore, in active geothermal systems very few studies report trace metal concentrations in pyrite (Reykjanes geothermal system; Libbey & William-Jones, 2016), and no data linking sulfide composition, paleofluid and present-day fluid chemistry are currently available. Such information is relevant and is feasible to obtain in a young, active geothermal system where fewer mineralization events are present, pyrite show fewer growth zones and/or chemical oscillations, and the reservoir fluid (i.e. ore-forming fluid) is accessible. This evidence is crucial to interpret the reportedly complex zoning of pyrite in fossil hydrothermal systems.

In this paper we report a comprehensive major and trace element database of pyrite from the active Tolhuaca Geothermal System (TGS) in the Andes of southern

Chile, a high enthalpy geothermal reservoir that has been drilled down to ~2 km depth, but has not affected by geothermal production or re-injection (Melosh et al., 2012; Sánchez-Alfaro et al., 2016a). At the TGS fine-grained pyrite is abundant, the present-day well fluid carry metals and metalloids including Cu, Au and As, among others, and paleofluids compositions are also available from fluid inclusions studies (Sánchez-Alfaro et al., 2016a). Therefore, the TGS provides an excellent opportunity to link the chemical and textural features of pyrite with paleofluids and borehole fluid composition data. In situ concentrations of precious metals (e.g., Au, Ag), metalloids (e.g., As, Sb, Se, Te) and base and heavy metals (e.g., Cu, Co, Ni, Pb) were measured using a combination of electron microprobe analysis (EMPA) and secondary-ion mass spectrometry (SIMS) in a suite of well constrained pyrite samples retrieved from a ~1 km drill core. Furthermore, we correlated our pyrite trace element data with geochemical data of present-day borehole fluid samples and LA-ICP-MS analyses of fluid inclusion assemblages hosted in paragenetically-linked quartz and calcite veins from Sánchez-Alfaro et al. (2016a). By integrating these three sources of data, i.e., elemental concentrations in pyrite, fluid inclusions data and borehole fluid chemistry, we provide evidence that fluctuations in the trace element budget of pyrite are directly linked to changes in hydrothermal fluid composition resulting from episodic inputs of magmatic vapor and/or phase separation (or boiling) of a single-phase hydrothermal fluid.

2. GEOLOGICAL BACKGROUND

In the Andean Cordillera of the central-southern Chile, hydrothermal systems occur in close spatial relationships with active volcanism as well as with major seismically active fault systems (Cembrano and Lara, 2009). In this region, geothermal features are spatially related with the Liquiñe-Ofqui Fault System and with the NW-trending Arc-oblique Long-lived Basement Fault System (Sánchez et al., 2013; Tardani et al., 2016). The active TGS is located in the northern termination of the Liquiñe-Ofqui Fault System (Fig. 1) and is spatially associated with both NE- and NW-striking faults.

The Tolhuaca volcano is a glacially scoured composite stratovolcano of late-Pleistocene to Holocene age that rises ~900 m over a Miocene volcano-sedimentary rock basement (Thiele et al., 1987; Lohmar et al., 2012). In the summit, several NW-trending aligned craters with different preservation states indicate a migration of the volcanic activity from the SE towards the NW (Thiele et al., 1987). Lavas are

predominantly basaltic andesites and andesites, with minor presence of basalts and dacites (Thiele et al. 1987; Lohmar et al., 2012). The latest eruptive phases occur in the NW portion of the volcanic edifice and correspond to a ~2 km long NW-trending fissure and a pyroclastic cone. The Tolhuaca volcano is likely to be related to the ALFS, which provides the suitable conditions for the development of magma reservoirs and magma differentiation (Cembrano and Lara, 2009; Pérez-Flores et al., 2016).

The TGS is located in the northwest flank of the Tolhuaca volcano and is characterized by several surficial thermal manifestations including fumaroles, boiling pools and hot springs (Fig. 1). Geothermal exploration campaigns have revealed the existence of a high-enthalpy reservoir in the system (Melosh et al., 2010; 2012). Two slim holes (Tol-1 and Tol-2) and two larger diameter wells (Tol-3 and Tol-4) were drilled down to 2117 m vertical depth (Fig. 1). Temperature logging and fluid samples suggest the presence of a geothermal reservoir at c.a. 1.5 km depth, at liquid-saturated conditions with temperatures up to 300 °C and a relatively high meteoric water component (Melosh et al., 2012). The main reservoir is overlain by a steam heated aquifer at shallow depths that reaches up to 160 °C and controls the chemical nature of most of the hot springs (Melosh et al., 2010; 2012).

The different geologic units, observed in the Tol-1 drill core material, are mainly lavas and related breccias, volcanoclastics and minor tuffs (Fig. 1). Hyaloclastites and pillow breccias also occur at different levels in the Tol-1 core (Lohmar et al., 2012; Sánchez-Alfaro et al., 2016a). Based on thin section petrography and X-ray diffraction (XRD) analyses of the Tol-1 core, three alteration zones were defined: 1) an upper zone of argillic alteration (20 to 450 m); 2) an intermediate zone with sub-propylitic alteration (450 to 650 m); and 3) a deeper zone of propylitic alteration (≥ 650 m) (Fig. 1) (Melosh et al., 2012). Lohmar et al. (2012) and Sánchez-Alfaro et al. (2016a) characterized argillic alteration facies by Fe-oxides + chlorite + calcite + clay + quartz + pyrite (+ apatite), whereas the mineral assemblages in high temperature propylitic facies are composed of chlorite + epidote + calcite + pyrite + quartz + zeolites.

Melosh et al. (2012) and Sánchez-Alfaro et al. (2016a) recognized four stages (S1 to S4) of hydrothermal alteration in the TGS. The S1 stage represents an early heating event characterized by precipitation of iron oxides, quartz, and chalcedony as a result of widespread boiling and flushing. An episode of pervasive hydrothermal alteration of the volcanic and volcaniclastic rocks defines the S2 stage, where low temperature (<200 °C) argillic alteration assemblages (smectite; illite/smectite;

interlayered chlorite/smectite, pyrite, calcite and chalcedony/amorphous silica) developed at the shallower levels (<670 m), while propylitic alteration assemblages (chlorite, epidote, quartz, calcite and pyrite) were formed under higher temperature (≥250 °C) conditions in the deep upflow zone (>700 m). Between the S2 and S3 stages, a low-permeability clay cap composed of chlorite and smectite was formed, separating the deep part of the system (propylitic alteration) from the shallower one (argillic alteration) (Fig. 1). The S3 stage was characterized by an increase in magmatic heat that promoted hydro-fracturing and brecciation of the clay-cap. The homogenization temperature data from fluid inclusions indicate diffuse boiling in the upper and lower zones. Finally, the S4 stage reveals a phase of fluid mixing and gentle boiling.

3. SAMPLES AND METHODS

Six representative pyrite-bearing samples from the argillic and propylitic alteration zones were selected (PFI-2, PFI-3, PFI-26, PFI-39, PFI-41, and PFI-45) from different depths of the drill core, as shown in Figure 1. Scanning electron microscope (SEM) observations were undertaken at the Andean Geothermal Centre of Excellence (CEGA), Universidad de Chile, using a FEI Quanta 250 SEM equipped with secondary electron (SE), energy-dispersive X-ray spectrometry (EDS), backscattered electron (BSE) and cathodoluminescence (CL) detectors. The analytical parameters were: spot size of 1-3 μm, an accelerating voltage of 10-20 keV, a beam intensity of 80 μA, and a working distance of 10 mm.

Pyrite is present as euhedral or sub-euhedral disseminated grains (<1 mm) at the TGS, occurring in millimeter-sized monomineralic veinlets and in micrometer-sized crystals in the rim of veins of amorphous silica and Fe-oxides (Fig. 2). Pyrite is generally fine-grained in the deeper propylitic zone (<30 μm). In the sub-propylitic zone (clay cap), pyrite is almost absent and is replaced by minor chalcopyrite and bornite. Minor amounts of sphalerite and galena are also identified. For detailed descriptions of the alteration and mineralization assemblages at Tolhuaca, the reader is referred to Sánchez-Alfaro et al. (2016a).

Electron microprobe analysis (EMPA) of pyrite grains (152 spot analyses total) was performed using a field-emission ~~gun~~ JEOL 8530F hyperprobe equipped with five wavelength-dispersive spectrometers at the Center for Microscopy, Characterization and Analysis (CMCA), University of Western Australia in Crawley, WA. Operating conditions were 40 degrees take-off angle and beam energy of 20 keV. The beam

current was 50 nA, and the beam was fully focused. Elements were acquired using the following analyzing crystals: LiF for Fe Kα, Au Lα, Te Lα, Cu Kα, Ni Kα, Zn Kα and Co Kα; PETJ for S Kα, Ag Lα, and Cd Lα; PETH for Sb Lα, and Pb Mα; and TAP for As Lα and Se Lα. The standards employed were commercially available metals, oxides, sulfides, selenides, and tellurides. Counting time was 20 seconds for S Kα and Fe Kα, 60 seconds for Cu Kα, Ni Kα, Zn Kα, and Co Kα, 80 seconds for Se Lα and Te Lα, 100 seconds for As Lα, Sb Lα, and Pb Mα, 120 seconds for Ag Lα and Cd Lα, and 200 seconds for Au Lα. Mean atomic number background corrections were employed throughout (Donovan and Tingle, 1996). Unknown and standard intensities were corrected for dead time and the ZAF algorithm was used for matrix absorption (Armstrong, 1988). On-peak interference corrections were applied as appropriate (Donovan et al., 1993). Detection limits ranged from 0.006 wt. % for Sb to 0.032 wt. % for Au.

Wavelength-dispersive spectrometry (WDS) X-ray maps were acquired using the calibration set up described above. Detection limit maps were acquired for these elements and applied as the minimum cut-off values. Map acquisition utilized a 100 nA beam current with 2 x 2 µm pixel dimension and 40 msec dwell time per pixel. Data were processed using the Calcimage software package and output to Surfer® for further processing and enhancement.

Additionally, 152 secondary-ion mass spectrometry (SIMS) spot analyses were acquired on individual pyrite grains from selected samples from the argillic and propylitic alteration zones (Table 2). SIMS analyses were performed at the Advanced Mineral Technology Laboratories (AMTEL) in London, Ontario, using a Cameca IMS-3f ion microprobe. Secondary ions monitored were ^{63}Cu, ^{65}Cu, ^{75}As, ^{78}Se, ^{80}Se, ^{107}Ag, ^{109}Ag, ^{121}Sb, ^{123}Sb, ^{128}Te, ^{130}Te, and ^{197}Au. In addition, the major sulfide-matrix constituent isotopes, ^{56}Fe and ^{34}S were monitored. A 10 kV and 8 nA primary Cs+ beam source was used for measurements, with a 4.5 kV accelerating voltage used for the negative secondary ions. The analytical spot size of the primary beam was ~25 µm; depth of analysis was 3.5-7.0 µm. Mineral standards used were produced experimentally by implanting a known dosage of the element of interest into the pyrite matrix using the Tandetron accelerator at the University of Western Ontario, Canada. The detection limits were ~0.03 ppm for Au, 3 ppm for As, 0.1 ppm for Cu, 0.02 ppm for Ag, 0.2 ppm for Sb, 0.01 ppm for Te, and 0.1 ppm for Se. For depth-concentration profiles, the minimum detectable size of sub-micron mineral inclusions was 500 nm at a

5 sec counting time. Thus, if more than one nanoparticle or inclusion is intercepted simultaneously, they register as a single particle in the depth profile.

4. RESULTS

Representative EPMA and SIMS analyses of pyrite are reported in Tables 1 and 2, respectively. A summary of the trace elements concentration in pyrite is presented in Figure 3. Back-scattered electron (BSE) images and quantitative WDS X-ray maps of representative samples from the shallow argillic alteration zone (PFI-2 and PFI-3) are shown in Figure 4, while Figure 5 displays WDS X-ray maps of pyrite grains from the deeper propylitic alteration zone (PFI-39 and PFI-41). Although no marked vertical variation in the trace element concentrations was generally observed in pyrite from the TGS, the average concentrations of some metals (Cu, Co, Pb, and Ni) and metalloids (As, Sb, Te) are slightly higher in the shallower argillic alteration zone (first 250 m of the drillcore).

Pyrite from the TGS is characterized by high concentrations of As, Pb and Cu, up to ~5 wt. %, ~2 wt. % and ~1.5 wt. %, respectively (Fig. 3). Cobalt and Sb contents are also relatively high and vary from 0.2 to ~10000 ppm and from ~0.3 to ~5000 ppm, respectively, spanning five orders of magnitude in concentration. Arsenic, Cu and Co show distinct zoning in the shallower argillic alteration zone (Fig. 4). WDS X-ray maps indicate that arsenic is enriched in the rims of pyrite crystals and depleted in the center (Fig. 4b, f, i, l and o), while Cu and Co show the opposite distribution with the highest concentrations found in the pyrite cores (Fig. 4c, d, g, j, k, m, n, p and q). WDS X-ray maps of fine-grained pyrite from the deeper, propylitic alteration zone (Figs. 5a-f) do not display the well-defined zonation patterns observed in pyrite grains from the argillic alteration zone samples. Only one pyrite grain from the propylitic zone shows As-enriched cores (Fig. 5a), although these higher concentrations do not correlate with increased Cu or Co (Fig. 5b and c).

Concentrations of Au in pyrite are detectable using SIMS. Only one data point was detected by EPMA with a concentration of 1500 ppm (Table 1). SIMS data show Au values that vary between 0.01 to ~10 ppm. Silver concentrations range between 0.07 and ~400 ppm, with one data point reaching ~0.5 wt. %. Cadmium, Ti and Se contents of pyrite range from a minimum of 200, 160 and 0.03 ppm, respectively, to maximum concentrations of 1000's of ppm. Nickel and Te concentrations vary between ~60 to 600 ppm, and ~0.01 to 500 ppm, respectively.

5. DISCUSSION

5.1 Mineralogical incorporation of metals and metalloids in pyrite from the TGS

Pyrite from the TGS can be classified as "arsenian" in terms of its As contents (i.e., up to 5 wt. % levels), which is also in agreement with the high As concentrations documented in the well fluids and thermal springs (up to 25 ppm; Sánchez-Alfaro et al., 2016a). The generally homogeneous distribution of As in pyrite, as detected by WDS X-ray maps (Figs. 4b, f, i, l, o and Figs. 5a and d), strongly suggests that As is structurally bound (solid solution), even if the As-Fe-S ternary diagram in Figure 6 suggests minor presence of As^0. Correlation plots showing As-S and As-Fe inverse trends (Figs. 7a and b) and the ternary diagram of Figure 6 does not show a conclusive trend of As substitution at the TGS, and it is likely that As^{1-}, As^{2+} and As^{3+} ionic species are present (Deditius et al., 2008; 2014; Qian et al., 2013). No significant clustering distribution of As are observed in WDS maps, where As is markedly enriched in the pyrite rims (Figs. 4b, f, i, l and o). Also, no noticeable differences in As speciation are observed in pyrite from the shallower or deeper zones, as suggested using SIMS depth profiling, where each successively deeper layer of the material is analyzed as a function of time. The flat ^{75}As depth profile in Figure 8b strongly suggests that As is mainly incorporated within the pyrite structure.

The high Cu concentrations (up to ~2 wt. %) measured by EMPA are related to two dominant mineralogical forms of Cu, as observed on SIMS depth profiles: (i) structurally bound Cu, and (ii) as micro- to nano-sized inclusions of chalcopyrite (Figs. 8c and d). Both forms of Cu can also be observed in the elemental maps in Figures 4d, g, k, n and q, and in Figures 5c and f. Structurally bound Cu is distributed homogeneously, forming the light blue-colored areas usually restricted to the core of the pyrite crystals, which contrasts with the dark-blue, low-Cu background (Fig. 4d, g and k, WDS maps). The elemental plot in Figure 7c shows a negative correspondence between Cu and Fe (R^2=0.60), suggesting $Cu^{2+} \Leftrightarrow Fe^{2+}$ as a possible substitution, although the precise mechanism of Cu incorporation cannot be deduced (Shimazaki and Clark, 1970; Schmid-Beurmann and Bente, 1995). It is likely that most of the structurally bound Cu replaces Fe in octahedral sites, which may be due to considerable distortion of the pyrite symmetry by the presence of other elements such as As, Sb or Co (Radcliffe and McSween, 1969; Bayliss, 1989).

Micro- to nano-sized Cu-bearing inclusions occur as scattered discrete particles and blebs along the growth zones (Fig. 4d, k, n and Fig. 5c; yellow-to-red-colored). The size of the particles is less than 5 μm, and they occur as individual inclusions and/or as aggregates of abundant micrometer- to submicrometer-sized particles. The occurrence of the two mineralogical forms of Cu in pyrite in the TGS is confirmed by SIMS depth profiling. In Figure 8c and d, depth–concentration profiles are presented for the pyrite matrix isotopes (^{56}Fe, ^{34}S) and copper (^{63}Cu). When Cu is present in solid solution (structurally bound), the depth–concentration profile of ^{63}Cu is flat (Fig. 8c, 1100 ppm Cu), whereas at higher concentrations the spiky ^{63}Cu profile confirms the presence of individual particles or clusters of particles of 500 nm in size (Fig. 8d, ~100 ppm Cu). Previous experimental studies have pointed out that the solid solution of CuS_2 in FeS_2 is thermodynamically unstable in nature and the solubility of Cu in FeS_2 decreases considerably with temperature (from 4.5 mol% Cu at 900 °C to ~0.6 mol% Cu at 700 °C, at 45 kbar; Shimazaki and Clark, 1970; Schmid-Beurmann and Bente, 1995). However, the solubility of Cu in pyrite has not been determined at the lower temperatures relevant for most hydrothermal systems (e.g., <500 °C). Analogously to Reich et al. (2005), it may be suggested that the incorporation of As could influence Cu incorporation in both solid solution and as Cu-bearing nanoparticles in pyrite (Reich et al., 2013). At the TGS, Cu and As concentrations do not show a correspondence (Fig. 7d), and the micrometric chalcopyrite inclusions are found associated with both low and high As-bearing concentration zones. At very low temperatures (i.e., sedimentary settings) Cu is incorporated within the pyrite structure at low concentrations (ppm levels), while Cu-bearing microinclusions at present at higher concentrations (wt % levels; Gregory et al., 2015a). Factor analysis has shown that Cu is associated with large cations that disrupt the pyrite structure enhancing Cu incorporation. However, it is likely that the total concentration of the metals in fluids play a key role on Cu incorporation into pyrite as evidenced in studies such as Gregory et al. (2015a).

As shown in Tables 1 and 2 and Figure 3, Co concentrations in pyrite are variable, ranging from hundreds of ppb to thousands of ppm. Despite the fact that the plot of Co-Fe in Figure 7e does not show a clear correlation trend, the SIMS depth profile (Fig. 8a) and WDS X-ray maps (Fig. 4c, j, m and p) suggest that cobalt in the studied pyrites is in solid solution. This is in agreement with the fact that Co extensively substitutes for Fe in pyrite, due to the similar ionic radii of Co^{2+} and Fe^{2+}, and that the CoS_2 endmember adopts the pyrite structure (Vaughan and Craig, 1978; Tossell et al.,

1981; Abraitis et al., 2004; Gregory et al., 2015a, b). WDS X-ray maps in Figure 4c, j, n, p, show that chemical zoning of Co, like Cu, is spatially correlated to cores and/or thin bands within pyrite crystals. The positive correspondence between Co and Cu in Figure 7f supports the hypothesis that these two metals may be included in pyrite in similar mineralogical form. The relatively high Co concentrations (up to ~0.2 wt. %) and high Co/Ni ratios between 1 and 10 in pyrite from the TGS (Fig. 9a) are indicative of a magmatic-hydrothermal origin associated with a greater mafic affinity (Large et al., 2009; Koglin et al., 2010; Reich et al., 2016), in agreement with the composition of the lavas from Tolhuaca volcano, which have mainly basaltic to andesitic compositions (Sánchez-Alfaro et al., 2016a).

Apart from the base metals, precious metal (Au, Ag) concentrations in the studied pyrite are at least one order of magnitude higher when compared to pyrite from other active geothermal systems (Libbey and William-Jones, 2016), ranging from 0.01's to 10's of ppm for Au and from 0.01's to 1000's of ppm for Ag (Tables 1 and 2). Gold and silver incorporation into pyrite structure is favored by the substitution of anionic or cationic As, due to a structural distortion and/or decrease in the size of pyrite grains, increasing the surface/volume ratio (e.g., Simon et al., 1999; Palenik et al., 2004; Deditius et al., 2008; 2014). Several different incorporation mechanisms for Au and As have been proposed for pyrite. The most validated model involves the coupled substitution of cationic Au for Fe in distorted octahedral sites and anionic As for S in tetrahedral sites (Simon et al., 1999). It is relevant to note that the highest concentrations of Au in pyrite are usually related to the presence of Au-bearing micro- to nano-sized inclusions and clusters of Au nanoparticles (Reich et al., 2005; Deditius et al., 2014; Gregory et al., 2015a; 2016).

As shown in Table 2 and Figure 3, SIMS data show Au concentrations in pyrite that varies between 0.01 and ~10 ppm. Only one EMPA data point reported in Table 1 shows Au concentration of 1500 ppm (sample PFI-41; Table 1). In Figure 9b, most Au–As analyses plot below the solubility limit defined by Reich et al. (2005), suggesting that Au occurs as structurally bound ions (Au^{1+}). Only three data points plot above the As-dependent solubility limit, indicating the presence of nanoparticles of native Au^0 and/or Au-tellurides. Although SIMS depth–concentration profiles do not confirm the presence of nanoinclusions (Fig. 8e and f), the occurrence of nanoparticles smaller than the SIMS depth-profiling detection capabilities (<500 nm) is possible, and higher concentrations of Au (e.g., >10 ppm) measured by EMPA and SIMS may be related to

micro- to nano-sized Au-bearing mineral particles. The similar incorporation behavior of Au and Te, both as solid solution or gold-telluride, is also assessed by the positive correlation between Au and Te, shown in Figure 9c.

As shown in Tables 1 and 2 and summarized in Figure 3, the measured Ag content of pyrite varies between ~0.07 and 5000 ppm. Previous studies have shown that Ag is widely present in pyrite in both solid solution (replacing Fe^{2+} as Ag^{+}) and/or forming micro and nano-sized Ag-sulfide and sulfosalt inclusions (Abraitis et al., 2004; Deditius et al., 2011). At the TGS, SIMS depth profiles show that Ag occurs in both mineralogical forms. In Figure 10a and b, depth–concentration profiles are presented for ^{109}Ag. The flat profile in Figure 10a (at 11 ppm Ag) support the presence of Ag in solid solution, whereas the spiky ^{109}Ag profile confirms the presence of individual particles or clusters of Ag-bearing particles <500 nm in size (Fig. 10b, 5 ppm Ag). The generally positive trend between Ag and Au (Figure 9d) suggests a similar incorporation behavior of these two metals, as documented in previous studies (e.g., Reich et al., 2010). Furthermore, Ag-As data points in Figure 9e show two groups at higher (~200 ppm) and lower (<100 ppm) Ag contents. The lower Ag concentration group display a positive correspondence with As, while the high-Ag concentrations do not vary with As contents, showing a line parallel to the Y axis. These data, in addition to SIMS depth profiles in Figure 10a and b, suggest that Ag incorporation into pyrite is dependent on As and follow a similar behavior than Au (Reich et al., 2005; 2013; Deditius et al., 2014).

All other trace elements measured in pyrite at the TGS (e.g. Pb, Ni, Ti, Sb, Se, Te, Cd) also occur in relatively high amounts, e.g., 100-ppm levels for Ni and Te, 1000-ppm levels for Ti, Sb, Se and Cd, and up to wt. % levels for Pb. Lead may be incorporated in solid solution by the substitution of Pb^{2+} for Fe^{2+}, as suggested by the negative relation shown in the elemental plot of Figure 9f. However, the high concentrations of Pb (up to 2 wt. %) may also be attributed to the presence of sub-micron sized Pb-bearing inclusions, most likely galena (Griffin et al., 1991; Huston et al., 1995; Abraitis et al., 2004; Pacevski et al., 2012; Gregory et al., 2015a). Tellurium and Se are likely hosted in solid solution, as shown in the flat SIMS profiles (Figs. 10c and d), although the presence of micro- or nano-inclusions cannot be excluded. In fact, the SIMS depth profiles in Figure 10e and f indicate that Se is probably incorporated in pyrite as both solid solution and Se-bearing mineral inclusions.

5.2 Decoupling of Cu and As in the TGS: linking pyrite chemistry with paleofluid and borehole fluid composition

The trace element geochemistry of pyrite has proven useful in accessing the history of complex processes undergone by a single sample. In magmatic-hydrothermal settings, pyrite has been used to fingerprint ore sources, vector towards mineralization and infer changes in fluid composition (e.g., Franchini et al., 2014; Mukherjee and Large, 2016). Similar observations are reported in lower temperature sedimentary environments where pore waters progressively enrich in trace elements as they desorb from organic matter, resulting in a sequential enrichment of trace elements in pyrite with increasing sediment depth (Huerta-Diaz and Morse, 1994; Gregory et al., 2014).

Abrupt changes in As and Cu concentrations in pyrite growth zones have been observed in the Pueblo Viejo and Yanacocha high sulfidation Au-Ag deposits (Deditius et al., 2009). Arsenic-rich zones, also enriched in Au, Ag, Sb, Te, and Pb, alternate with Cu-rich zones with significantly lower concentrations of these elements and barren pyrite zones with no other elements. In situ trace element and sulfur isotope ($\delta^{34}S$) data by Peterson and Mavrogenes (2014) in pyrite at the Porgera Au deposit in Papua New Guinea uncovered a stratigraphy of repeated high-Au negative $\delta^{34}S$ and low-Au positive $\delta^{34}S$ zones, recognized with a 3 µm spot size laser ablation, within individual pyrite crystals present in the highest grade gold event. These zonations are less likely to reflect changes in substitutional mechanisms of As and Cu into pyrite forming from a fluid of constant composition. Rather, the chemical and isotopic data provide strong evidence pointing to sharp variations in the pyrite-forming fluid composition (Deditius et al., 2009; Kouzmanov et al., 2010).

In high-temperature hydrothermal settings, these abrupt chemical changes have been interpreted as the result of mixing between the pyrite-forming fluids and magmatic vapors, the latter capable of geochemically decoupling As and Cu during its separation from the parental magma (Deditius et al., 2009). Indeed, although it has been observed that both As and Cu partition into the magmatic vapor, they respond differently to P-T-X conditions of the system, especially in terms of ligands (Cl and S) availability (Heinrich et al., 1999; 2004; Pokrovski et al., 2002; 2005; Williams-Jones et al., 2002; Williams-Jones and Heinrich, 2005; Simon et al., 2006; 2007; Pokrovski et al., 2013). Magmatic vapors, formed by direct separation from the parental silicate magma, may remain a single phase or separate into a brine and a lower density vapor, a process that can take place more than once during the upward migration of the magmatic vapor

(Heinrich, 2004, 2005). These phase separation processes are capable of fractionating As and Cu in the porphyry-epithermal environment. Pokrovski et al. (2005; 2013) compiled experimental data of vapor-liquid partition coefficients between 300 and 450 °C for various metalloids, base and precious metals. They determined that As partitions preferentially into the low density, low salinity vapor phase than Cu which has a higher affinity for the high-density saline brine. This selective metal partitioning has been extensively reported in experiments and fluid inclusion studies in ore deposits, from the deeper magmatic-hydrothermal porphyry roots to the shallower epithermal domain (Kouzmanov and Pokrovski, 2012, and references therein).

For most hydrothermal systems it remains difficult to determine how the compositions of hydrothermal fluids change with time and how those changes affect the precipitation of ore minerals, including pyrite (Rusk et al., 2008). Several studies have reported LA-ICP-MS data of fluid inclusions from porphyry systems (e.g., Heinrich et al., 2005; Audetat et al., 2008), epithermal Au(-Ag) deposits (e.g., Pudak et al., 2009), and from fluid inclusions hosted in sulfide ore minerals (e.g., Wilkinson et al., 2009; Kouzmanov et al., 2010). All these studies have reported significant variations in metal concentrations related to chemical fluctuation of hydrothermal ore fluids. Despite such evidence, a direct correlation between chemical changes in ore-forming fluids and the trace metal chemical zonations recorded in pyrite (e.g. Cu, As, Co, Au, Sb, Ni) remains to be confirmed beyond trace element analyses of the sulfide phase (Large et al., 2009; Deditius et al., 2009; Thomas, 2011; Reich et al., 2013; 2016; Peterson and Mavrogenes, 2014; Deditius et al., 2014; Steadman, 2015; Gregory et al., 2016).

By combining our EMPA/SIMS pyrite data with 1) LA-ICP-MS analyses of fluid inclusion that are paragenetically linked in calcite/quartz veins, and 2) borehole fluid chemical data at the TGS, we provide evidence that the observed zonations in pyrite are likely related to chemical changes in the pyrite-forming hydrothermal fluid. Borehole fluids in the TGS have trace metal contents that are broadly similar to those measured in the Taupo Volcanic Zone in New Zealand and in the active Lihir gold deposit in Papua New Guinea (Simmons and Browne, 2000; Simmons et al., 2016a, b; Sánchez-Alfaro et al., 2016b). Furthermore, and unlike pyrites from ore deposits that commonly show multiple growth bands and complex oscillatory zoning patterns, pyrite in the shallow argillic zone of the TGS presents the advantage of having only two growth zones as observed in the WDS X-ray maps (Figures 4 and 11).

The fluid inclusions data used in this study were reported by Sánchez-Alfaro et al. (2016a). In particular, the LA-ICP-MS data were obtained in fluid inclusion assemblages observed in pyrite-bearing, calcite/quartz veins retrieved from the shallower part of the drillcore (first 400 m), which represents the upwelling paleo-hydrothermal fluid. In contrast, the present-day borehole fluid composition (measured using ICP-MS) is likely to represent the resulting fluid after the condensation of a low-density vapor that separated from a magmatic-hydrothermal fluid sourced in the deeper parts of the hydrothermal system. This distinction allows us to correlate the composition of paleo- and present-day fluids with measured concentrations of trace metals in cores and rims of pyrite in the shallow argillic zone, which are the only pyrite grains that show clear zonation patterns.

As shown in Figure 11a and b, we will refer in the following discussion to the pyrite growth zones as P1 for pyrite cores, and P2 for the pyrite rims. Copper-As ratios of pyrite cores (red) and rims (green) are compared in Figure 11c with the Cu/As ratios of fluid inclusions (red circles) and borehole fluid from the TGS (green circles). The textural and chemical data in Figure 11 suggest that a Cu-rich, As-depleted fluid was involved in pyrite core formation (P1), followed by a late-stage, low-Cu and high-As fluid related to the precipitation of pyrite rims (P2). In the same way, the comparison between (present-day) borehole fluids and fluid inclusion data reveals significant differences. Fluid inclusions are Cu-rich but poor in As (Cu/As~1) while borehole fluids are rich in As, but Cu-poor (Cu/As~10^{-3}). According to Sánchez-Alfaro et al. (2016a), simple boiling models cannot explain the aforementioned differences in fluid chemistry because non-volatile elements such as Cu and As remain in the liquid phase during boiling ($K_d=C_{vapor}/C_{liquid}$, K_{As}=0.001-0.01; $K_{Cu}< 10^{-3}$; $K_{Na}<10^{-3}$) under epithermal conditions (100<T<280 °C; Pokrovski et al., 2013). In Figure 11, the relatively high-Cu, low-As concentrations in fluid inclusions (Cu/As~1, Fig. 11c) can be paragenetically linked to the formation of the Cu-rich, As-depleted pyrite cores (Cu/As~1-10, Fig. 11c). In contrast, the As-rich, Cu-depleted pyrite rims (Cu/As~0.1-0.01, Fig. 11c) correlate with the high-As and low-Cu concentrations measured in the borehole fluid (Cu/As~10^{-3}, Fig. 11c) at the TGS. These observations strongly suggest that the zonations reported in pyrite from TGS are the result of a compositional change of the pyrite-forming hydrothermal fluid during continuous pyrite precipitation.

EMPA data and WDS X-ray maps also show that pyrite cores are significantly enriched in Co (up to 4 wt. %). Unfortunately, no experimental partitioning data are

available for Co, and Sánchez-Alfaro et al. (2016a) do not report Co concentrations in fluid inclusion or borehole fluids. However, and as shown by Pokrovski et al. (2013), most base metals present a marked affinity for a high-density saline brine; therefore it is reasonable to assume that Co may display a similar behavior than Cu (see maps in Fig. 4c, j, m and p).

The pyrite core precipitation stage P1 at Tolhuaca was most likely related to Cu(Co)-rich supercritical magmatic vapors that segregated during a stage of magmatic diking and sill intrusion as reported for the TGS. The episodic separation of these magmatic vapors produced fluid overpressure conditions inducing fracturing and brecciation of the low permeability clay-cap, as observed by Sánchez-Alfaro et al. (2016a). This magmatically derived single-phase fluid ascended, and following phase separation (or boiling) (Sánchez-Alfaro et al., 2016b), precipitated pyrite (cores) with high concentrations of Cu and Co, in both the deep and shallower parts of the TGS. Pyrite in the argillic (shallower) zone hosts higher concentrations of Cu and Co than pyrite in the propylitic (deeper) zone (Fig. 3; Tables 1 and 2). This may be due to the neutralization of acid hydrothermal fluids in the upper argillic zone, as proposed by Sánchez-Alfaro et al. (2016a), producing a concomitant decrease of metal solubility in the fluid phase.

During a later phase of evolution of the TGS (P2), the fluid pressure was lower than the lithostatic pressure and the clay-cap acted as a low-permeability barrier (Sánchez-Alfaro et al., 2016a). Phase separation took place in the deeper part of the system, partitioned the magmatic/hydrothermal fluid into a low-density vapor and high-density brine capable of fractionating Cu (and Co) and As. During this phase, only the As-rich vapor was able to migrate upwards, reaching the dominantly-meteoric aquifer in the argillic zone and possibly contracting into an As-rich hydrothermal fluid that precipitated the As-rich, Cu(Co)-poor pyrite rims, over the previously formed Cu(Co)-rich, As-depleted cores (Fig 4f, g, i, k, o and q). The Cu(Co)-rich, As-poor brine, on the other hand, remained in the deep (propylitic) part of the system where it continued precipitating pyrite with similar Cu, Co and As concentrations as the pyrite core deposited during P1 phase. In the sub-propylitic zone, the local accumulation of the brine, now blocked by the low permeability barrier or clay-cap, may have triggered local supersaturation of Cu in the fluid phase with the consequent deposition of chalcopyrite and bornite instead of pyrite as the main sulfide phase.

Our results are in agreement with recent studies discussed by Simmons et al. (2016a, b) in the Taupo Volcanic Zone, New Zealand, where significant amounts of metals are reported in geothermal fluids. The authors report that boiled chloride waters are strongly depleted in Cu, Pb, Ag, Au, and Te, because these metals deposit in sharp response to gas loss and cooling in the well. In contrast, As, Sb, and other metals and metalloids are measurably less depleted in boiled waters, making them available to form metal anomalies at shallow depths (Simmons et al., 2016a, b).

The precipitation of Cu minerals might have also been reached locally in the argillic zone during the P2 phase. As previously documented, kinetic effects can trigger the formation of micro to nano-particulate inclusions of chalcopyrite that co-precipitate with pyrite during rim formation (Fig. 4k and n) (Deditius et al., 2011; Reich et al., 2011). Therefore, Cu-bearing nanoparticle nucleation in pyrite might be, in this case, favored by the high As concentration on the mineral surface, or electrochemical effects as it has been previously proposed for precious and base metals (e.g., Au, Ag, Pb and Zn) (Oberthur et al., 1997; Abraitis et al., 2004; Mikhlin et al., 2007; 2011).

6. CONCLUDING REMARKS

Our EMPA–SIMS database show that significant concentrations of base and heavy metals (e.g., Cu, Co, Ni, Pb), precious metals (e.g., Au, Ag) and metalloids (e.g., As, Te, Se, Sb) are hosted in pyrite at the Tolhuaca Geothermal System. Detailed WDS X-ray maps and SIMS depth vs. isotope concentration profiles reveal that pyrites in the shallower argillic zone in the TGS are characterized by two chemically distinct zones where Cu(Co) and As are geochemically decoupled, while pyrites in the deeper part of the system (propylitic zone) do not display significant textural or chemical zonations.

When contrasting Cu-As contents in pyrite cores and rims with LA-ICP-MS fluid inclusion data and borehole fluid composition (Sánchez-et al., 2016) in the TGS, we observed that selective partitioning of metals and metalloids into pyrite is most likely the result of changes in fluid composition. The aforementioned changes are interpreted as being related to excursions of single-phased, magmatically-derived vapors that are further separated into a low-density vapor and dense brine capable of selectively scavenging Cu and As. During the first stage of pyrite formation (P1), fracturing of the impermeable clay-cap resulted in the formation of Cu(Co)-rich, As-depleted pyrite cores in both the deep and shallower parts of the TGS. This stage preceded the formation of As-rich Cu(Co)-depleted pyrite rims (P2) in the shallower (argillic) part of

599 the system. Although the absolute timing between these two main (and consecutive)
600 pyrite formation events is yet to be constrained, the high As and low Cu contents of the
601 present-day borehole fluids suggest that the late-stage, pyrite-forming fluids were
602 compositionally similar to the present-day fluid in the Tolhuaca deep reservoir.

603 The results presented in this study show that significant variations in fluid
604 composition may be related to abrupt changes in the P-T-X conditions at the TGS.
605 However, experimental studies and more observations in natural systems are needed to
606 assess the precise nature of the triggers leading to such changes – i.e., magmatic input
607 of metal rich fluids, system overpressure, and externally-forced perturbations such as
608 earthquakes (e.g., Cox and Ruming, 2004; Peterson and Mavorgenes, 2014, and
609 Sánchez-Alfaro et al., 2016b). Finally, results from this work confirm that pyrite
610 composition and micro-textures are valuable complements to other geochemical tools
611 used to investigate the evolution of hydrothermal systems.
612

613 **ACKNOWLEDGEMENTS**

614 This study was funded by FONDECYT grant #1130030 to Martin Reich.
615 Additional funding was provided through the MSI "Millennium Nucleus for Metal
616 Tracing Along Subduction" (NC130065) and FONDAP project 15090013 "Centro de
617 Excelencia en Geotermia de los Andes, CEGA". We would like to acknowledge as well
618 support from the Australian Microscopy & Microanalysis Research Facility at the
619 Centre for Microscopy, Characterisation & Analysis, University of Western Australia.
620 Daniele Tardani thanks financial support provided by the MECESUP program through a
621 Ph.D. scholarship. Finally, we acknowledge chief editor Marc Norman and associate
622 editor Weidong Sun for handling the manuscript. Daniel Gregory and two more
623 anonymous reviewers are acknowledged for their helpful comments and suggestions
624

625 **REFERENCES**

626 Abraitis P. K., Pattrick R. A. D., Vaughan D. J. (2004) Variations in the compositional,
627 textural and electrical properties of natural pyrite: a review. Int. J. Miner. Process. **74**,
628 41–59.

629 Aravena D., Muñoz M., Morata D., Lahsen A., Parada M. A., Dobson P. (2016)
630 Assessment of high enthalpy geothermal resources and promising areas of Chile.
631 Geothermics **59**, 1–13. doi:10.1016/j.geothermics.2015.09.001.

632 Armstrong J. T. (1988) Quantitative analysis of silicates and oxide minerals:
633 Comparison of Monte-Carlo, ZAF and Phi-Rho-Z procedures, in Newbury, D.E., ed.,
634 Microbeam analysis: San Francisco, CA, San Francisco Press, 239–246.

635 Audetat A., Pettke T., Heinrich C. A. and Bodnar R. J. (2008) The composition of
636 magmatic-hydrothermal fluids in barren and mineralized intrusions. Econ. Geol. **103**, 1–
637 32.

638 Bajwah Z. U., Secombe P. K., and Offler R. (1987) Trace element distribution, Co:Ni
639 ratios and genesis of the Big Cadia iron-ore deposit, New South Wales, Australia Miner.
640 Deposita **22**, 292–300.

641 Baker T., Mustard R., Brown V., Pearson N., Stanley C. R., Radford N. W., and Butler I.
642 (2006) Textural and chemical zonation of pyrite at Pajingo: A potential vector to
643 epithermal gold veins. Geochem. Explor. Environ. Anal. **6**, 283–293.

644 Barker S. L. L., Hickey K. A., Cline J. S., Dipple G. M., Kilburn M. R., Vaughan J. R.
645 and Longo A. A. (2009) Uncloaking invisible gold: use of nano-SIMS to evaluate gold,
646 trace elements, and sulphur isotopes in pyrite from Carlin-type gold deposits. Econ.
647 Geol. **104**, 897–904.

648 Bayliss P. (1989): Crystal chemistry and crystallography of some minerals within the
649 pyrite group. Am. Mineral. **74**, 1168-1176.

650 Belousov I., Large R., Meffre S., Danyushevsky L., and Beardsmore T. (2014) Pyrite
651 trace element compositions for ore deposits from Western Australia [abs.]. Goldschmidt
652 Conference, Sacramento, California, Abstracts, 167.

653 Berner, Z., Pujol, F., Neumann, T., Kramar, U., Stüben, D., Racki, G., and Simon, R.
654 (2006) Contrasting trace element composition of diagenetic and syngenetic pyrites:
655 implications for the depositional environment. *In* Proceedings Geophysical Research
656 Abstracts **8**, 08281.

657 Berner, Z. A., Puchelt, H., Noltner, T., and Kramar, U. T. Z. (2013) Pyrite geochemistry
658 in the Toarcian Posidonia Shale of south-west Germany: Evidence for contrasting trace-
659 element patterns of diagenetic and syngenetic pyrites. Sedimentology **60**, no. 2, 548-

573.

Bralia A., Sabatini G., and Troja P. (1979) A reevaluation of the Co/Ni ratio in pyrite as geochemical tool in ore genesis problems. Miner. Deposita **14**, 353–374.

Campbell F. A, and Ethier V. G. (1984) Nickel and cobalt in pyrrhotite and pyrite from the Faro and Sullivan orebodies. Can. Mineral. **22**, 503–506.

Cembrano J. (1996) The Liquiñe Ofqui fault zone: a long-lived intra-arc fault system in 800 southern Chile. Tectonophysics **259**, 55–66.

Cembrano J. and Lara L. (2009) The link between volcanism and tectonics in the southern volcanic zone of the Chilean Andes: A review. Tectonophysics **471**, 96–113

Chryssoulis S. (1990) Detection and quantification of "invisible" gold by microprobe techniques, in Hausen, D.M., Halbe, D.N., Petersen, E.U., and Tafuri, W.J., eds., Proceedings Symposium Gold 90: Littleton, CO, Society for Mining, Metallurgy, and Exploration, 323–331.

Ciobanu C. L., Cook N. J., Utsunomiya S., Kogagwa M., Green L., Gilbert S. and Wade B. (2012) Gold-telluride nanoparticles in arsenic-free pyrite. Am. Mineral. **97**, 1515–1518.

Cline J. S. (2001) Timing of gold and arsenic sulfide mineral deposition at the Getchell Carlin-type gold deposit, North- Central Nevada. Econ. Geol. **96**, 75–89.

Cook N.J. and Chryssoulis S.L. (1990) Concentrations of invisible gold in the common sulfides. Can. Mineral. **28**, 1–16.

Cook N. J., Ciobanu C. L. and Mao J. (2009) Textural controls on gold distribution in As-free pyrite from the Dongping, Huangtuliang and Hougou gold deposits, North china Craton (Hebei Province, China). Chem. Geol. **264**, 101–121.

Cox M. E., Browne P.R.L. (1995) The occurrence of pyrrhotite in the Ngawha geothermal system, New Zealand. Proc. New Zealand Geotherm. Workshop **17**, 35–40.

Cox, S.F., and Ruming, K. (2004) The St. Ives mesothermal gold system, Western

686 Australia—a case of golden aftershocks? J. Struct. Geol. **26**, 1109–1125.

687 Deditius A. P., Utsunomiya S., Renock D., Ewing R. C., Ramana C. V., Becker U.,
688 Kesler S. E. (2008) A proposed new type of arsenian pyrite: composition, nanostructure
689 and geological significance. Geochim. Cosmochim. Acta **72**, 2919–2933.

690 Deditius A. P., Utsunomiya S., Ewing R. C., Chryssoulis S. L., Venter D. and Kesler S.
691 E. (2009a) Decoupled geochemical behavior of As and Cu in hydrothermal systems.
692 Geology **37**, 707–710.

693 Deditius A. P., Utsunomiya S., Ewing R. C. and Kesler S. E. (2009b) Nanoscale "liquid"
694 inclusions of As–Fe–S in arsenian pyrite. Am. Mineral. **94**, 391–394.

695 Deditius A., Utsunomiya S., Kesler S. E., Reich M. and Ewing R. C. (2011) Trace
696 elements nanoparticles in pyrite. Ore Geol. Rev. **42**, 32–46.

697 Deditius A., Reich M., Kesler S.E., Utsunomiya S., Chryssoulis S., Walshe J.L., Hough
698 R., and Ewing R.C. (2014) The coupled geochemistry of Au and As in pyrite from
699 hydrothermal ore deposits. Geochim, Cosmochim. Acta **140**, 644–670

700 Donovan J. J., and Tingle T. N. (1996) An improved mean atomic number correction for
701 quantitative microanalysis. J. Micros. **2, 1**, 1–7.

702 Donovan J. J., Snyder D. A., and Rivers M. L. (1993) An improved interference
703 correction for trace element analysis. Microbeam Anal. **2**, 23–28.

704 Emsbo P., Hofstra A. H., Lauha E. A., Griffin G. L. and Hutchinson R. W. (2003) Origin
705 of high-grade gold ore, source of ore fluid components, and genesis of the Miekle and
706 neighboring Carlin-type deposits, Northern Carlin Trend, Nevada. Econ. Geol. **98**,
707 1069–1105.

708 Fleet M. E., Chryssoulis S. L., Maclean P. J., Davidson R.,Weisener G. (1993) Arsenian
709 pyrite from gold deposits: Au and As distribution investigated by SIMS and EP, and
710 color staining and surface oxidation by XPS and LIMS. Can. Miner. **31**, 1–17.

711 Franchini M., McFarlane C., Maydagán L., Reich M., Lentz D. R., Meinert L., and
712 Bouhier V. (2015) Trace metals in pyrite and marcasite from the Agua Rica porphyry-

713 high sulfidation epithermal deposit, Catamarca, Argentina: Textural features and metal
714 zoning at the porphyry to epithermal transition. Ore Geol. Rev. **66**, 366–387.

715 Griffin W. L., Ashley P. M., Ryan C. G., Soey H. S., Suter G. F. (1991) Pyrite
716 geochemistry in the North Arm epithermal Ag–Au deposit, Queensland, Australia: a
717 proton-microprobe study. Can. Mineral. **29**, 185–198.

718 Gregory, D., Meffre, S., and Large, R. (2014) Comparison of metal enrichment in pyrite
719 framboids from a metal-enriched and metal-poor estuary. Am. Mineral. **99**, no. 4, 633-
720 644.

721 Gregory, D. D., Large, R. R., Halpin, J. A., Baturina, E. L., Lyons, T. W., Wu, S.,
722 Danyushevsky, L., Sack, P. J., Chappaz, A., and Maslennikov, V. V. (2015a) Trace
723 Element Content of Sedimentary Pyrite in Black Shales. Econ. Geol. **110**, no. 6, 1389-
724 1410.

725 Gregory, D. D., Large, R. R., Halpin, J. A., Steadman, J. A., Hickman, A. H., Ireland, T.
726 R., and Holden, P. (2015b) The chemical conditions of the late Archean Hamersley
727 basin inferred from whole rock and pyrite geochemistry with d33 S and d34 S isotope
728 analyses. Geochim. Cosmochim. Acta **149**, 223-250.

729 Gregory, D. D., Large, R. R., Bath, A. B., Steadman, J. A., Wu, S., Danyushevsky, L.,
730 Bull, S. W., Holden, P., and Ireland, T. R. (2016) Trace Element Content of Pyrite from
731 the Kapai Slate, St. Ives Gold District, Western Australia. Econ. Geol. **111**, no. 6, 1297-
732 1320.

733 Günther, D., Audétat, A., Frischknecht, R., Heinrich, C.A. (1998) Quantitative analysis
734 of major, minor and trace elements in fluid inclusions using laser ablation-inductively
735 coupled plasmamass spectrometry. J. Anal. At. Spectrom. **13**, 263–270

736 Heinrich C. A. (2007). Fluid – fluid interactions in hydrothermal ore formation. Rev.
737 Mineral. Geochem. **65**, 363–387.

738 Heinrich C. A., Gunther D., Audetat A., Ulrich T. and Frischknecht R. (1999) Metal
739 fractionation between magmatic brine and vapor, determined by microanalysis of fluid
740 inclusions. Geology **27**, 755–758.

741 Heinrich C. A., Driesner T., Stefansson A. and Seward T. M. (2004) Magmatic vapour
742 contraction and the transport of gold from porphyry environment to epithermal ore
743 deposits. Geology **32**, 761–764.

744 Heinrich C. A., Halter W. E. and Pettke T. (2005) The formation of economic porphyry
745 copper (gold) deposits: constraints from microanalysis of fluid and melt inclusions. In
746 Mineral Deposits and Earth Evolution (ed. I. McDonald, et al.). Geol. Soc. (London)
747 Spec. Publ. **248**, 247–263.

748 Huerta-Diaz, M. A., and Morse, J. W. (1992) Pyritization of trace metals in anoxic
749 marine sediments. Geochim. Cosmochim. Acta **56**, 7, 2681-2702

750 Hulen J. B., Norton D. L., Moore J. N., Kaspereit D. (2004) Epithermal vein-hosted and
751 stratabound Pb–Zn mineralization in an active hydrothermal system: the southern Salton
752 Sea geothermal field, California. Geotherm. Resour. Counc. Trans. **28**, 415–424.

753 Huston D.L., Sie S.H., Suter G.F., Cooke D.R., and Both R.A. (1995) Trace elements in
754 sulfide minerals from eastern Australian volcanic-hosted massive sulfide deposits: Part
755 I. Proton microprobe analyses of pyrite, chalcopyrite, and sphalerite, and Part II.
756 Selenium levels in pyrite: Comparison with δ34S values and implications for the source
757 of sulfur in volcanogenic hydrothermal systems. Econ. Geol. **90**, 1167–1196.

758 Koglin N., Frimmel H.F., Lawrie Minter W.E. and Bratz H. (2010) Trace-element
759 characteristics of different pyrite types in Mesoarchean to Paleoproterozoic placer
760 deposits. Miner. Deposita **45**, 259–280.

761 Koseki T., Kazuo N. (2006) Sulfide minerals and sulfur isotope compositions from
762 wells MT-1 and MT-2 in the Bajawa Geothermal Field, Flores Island, Indonesia. J.
763 Geotherm. Res. Soc. Jpn. **28**, 223–236.

764 Koseki T., Nakashima K. (2006) Geothermal structure and feature of sulfide minerals of
765 the Mataloko geothermal field, Flores Island, Indonesia. Proc. of the Asian Geothermal
766 Symposium. **7**, 105–109.

767 Kouzmanov K., Pettke T. and Heinrich C.A. (2010). Direct analysis of ore-precipitating
768 fluids: combined IR microscopy and LA-ICP-MS study of fluid inclusions in opaque

769 ore minerals. Econ. Geol. **105**, 351–373.

770 Kouzmanov, K. and Pokrovski, G. (2012) Hydrothermal Controls on Metal Distribution
771 in Porphyry Cu (-Mo-Au) Systems. Society of Economic Geologists, Inc. Special
772 Publication **16**, 573–618.

773 Krupp R.E., Seward T.M. (1987) The Rotokawa geothermal system, New Zealand; an
774 active epithermal gold-depositing environment. Econ. Geol. **82**, 1109–1129.

775 Large R.R., Danyushevsky L., Hollit C., Maslennikov V., Meffre S., Gilbert S., Bull S.,
776 Scott R., Emsbo P., Thomas H., Singh B., and Foster J. (2009) Gold and trace element
777 zonation in pyrite using a laser imaging technique: Implications for the timing of gold in
778 orogenic and Carlin-style sediment-hosted deposits. Econ. Geol. **104**, 635–668.

779 Large, R. R., Halpin, J. A., Danyushevsky, L. V., Maslennikov, V. V., Bull, S. W., Long,
780 J. A., Gregory, D. D., Lounejeva, E., Lyons, T. W., and Sack, P. J. (2014) Trace element
781 content of sedimentary pyrite as a new proxy for deep-time ocean-atmosphere
782 evolution. Earth Planet. Sci. Lett. **389**, 209-220.

783 Large, R. R., Halpin, J. A., Lounejeva, E., Danyushevsky, L. V., Maslennikov, V. V.,
784 Gregory, D., Sack, P. J., Haines, P. W., Long, J. A., and Makoundi, C. (2015a) Cycles of
785 nutrient trace elements in the Phanerozoic ocean. Gond. Res. **28**, 1282–1293.

786 Large, R.R., Gregory, D.D., Steadman, J.A., Tomkins, A.G., Lounejeva, E.,
787 Danyushevsky, L.V., Halpin, J.A., Maslennikov, V.V., Sack, P.J., Mukherjee, I., Berry,
788 R., Hickman, A. (2015b) Gold in the oceans through time. Earth Planet. Sci. Lett. **428**,
789 139–150.

790 Lavenu A., Cembrano J. (1999). Compressional- and transpressional-stress pattern for
791 Pliocene and Quaternary brittle deformation in fore arc and intra-arc zones (Andes of
792 Central and Southern Chile). J. Struct. Geol. **21**, 1669–1691.

793 Libbey R.B., Williams-Jones A.E., Melosh B.L., Backeberg N.R. (2015)
794 Characterization of geothermal activity along the North American–Caribbean Plate
795 boundary in Guatemala: The Joaquina geothermal field. Geothermics **56**, 17–34.

796 Libbey R.B., Williams-Jones A.E. (2016) Relating sulfide mineral zonation and trace

797 element chemistry to subsurface processes in the Reykjanes geothermal system, Iceland.
798 J. Volcanol. Geoth. Res. **310,** 225–241.

799 Loftus-Hills G., and Solomon M. (1967) Cobalt, nickel and selenium in sulphides as
800 indicators of ore genesis. Miner. Deposita **2**, 228–242.

801 Lohmar S., Stimac J., Colvin A., González A., Iriarte S., Melosh G., Wilmarth M.
802 (2012) Tolhuaca volcano (Southern Chile, 38.3°S): New learnings from surface
803 mapping and geothermal exploration wells. In Proceedings Congreso Geológico
804 Chileno 2012 Antofagasta, Chile, 5-9. 443–445.

805 Long, J.A., Large, R.R., Lee, M.S.Y., Benton, M.J., Danyushevsky, L.V., Chiappe,
806 L.M., Halpin, J.A., Cantrill, D., Lottermoser, B. (2015) Severe selenium depletion in the
807 Phanerozoic oceans as a factor in three global mass extinctions. Gond. Res. **36**, 209–
808 218.

809 McKibben M.A., Elders W.A. (1985) Fe–Zn–Cu–Pb mineralization in the Salton Sea
810 geothermal system, Imperial Valley, California. Econ. Geol. **80**, 539–559.

811 McKibben M. A., Andes J. P., Williams A. E. (1988a) Active ore formation at a brine
812 interface in metamorphosed deltaic lacustrine sediments; the Salton Sea geothermal
813 system, California. Econ. Geol. **83**, 511–523.

814 McKibben M.A., Eldridge C.S., Williams A.E. (1988b) Sulfur and base metal transport
815 in the Salton Sea geothermal system. Geotherm. Resour. Counc. Trans. **12**, 121–125.

816 Melosh G., Cumming W., Benoit D., Wilmarth M., Colvin A., Winick J., Soto E.,
817 Sussman D., Urzúa-Monsalve L., Powell T., Peretz A. (2010) Exploration results and
818 resource conceptual model of the Tolhuaca Geothermal Field, Chile, in: Proceedings
819 World Geothermal Congress, Bali, Indonesia, 25-29 April 2010.

820 Melosh G., Moore J., Stacey R. (2012) Natural reservoir evolution in the Tolhuaca
821 geothermal field, southern Chile, in: 37th Workshop on Geothermal Reservoir
822 Engineering Stanford University, Stanford, California, January 31 - February 1, 881
823 2012. SGP-TR-194.

824 Meyer F. M., Oberthür T., Robb L.J., Saager R., and Stupp H.D. (1990) Cobalt, nickel

and gold in pyrite from primary gold deposits and Witwatersrand reefs. S. Afr. J. Geol. **93**, 70–82.

Mikhlin, Y.L., and Romanchenko, A.S. (2007) Gold deposition on pyrite and the common sulfide minerals: an STM/STS and SR-XPS study of surface reactions and Au nanoparticles. Geochim. Cosmochim. Acta **71**, 5985–6001.

Mikhlin, Y., Romanchenko, A., Likhatski, M., Karacharov, A., Erenburg, S., and Trubina, S. (2011) Understanding the initial stages of precious metals precipitation: Nanoscale metallic and sulfidic species of gold and silver on pyrite surfaces. Ore Geol. Rev. **42**, 47-54.

Mookherjee A., and Philip R. (1979) Distribution of copper, cobalt and nickel in ores and host-rocks, Ingladhal, Karnataka, India. Miner. Deposita **14**, 33–55.

Morey A.A., Tomkins A.G., Bierlin F.P., Wienberg R.F. and Davidson G. J. (2008) Bimodal distribution of gold in pyrite and arsenopyrite: Examples from the Archean Boorara and Bardoc shear systems, Yilgarn craton, Western Australia. Econ. Geol. **103**, 599–614.

Mukherjee, I., and Large, R. R. (2016) Application of Pyrite Trace Element Chemistry to Exploration for SEDEX Style Zn-Pb Deposits: McArthur Basin, Northern Territory, Australia. Ore Geol. Rev. (in press) http://dx.doi.org/10.1016/j.oregeorev.2016.08.004.

Oberthur T., Cabri L.J., Weiser T.W., McMahon G., Muller P. (1997) Pt, Pd and other trace elements in sulfides of the main sulfide zone, Great Dyke, Zimbabwe: a reconnaissance study. Can. Mineral. **35**, 597–609.

Pacevski A., Moritz R., Kouzmanov K., Marquart K., Zivkovic P. and Cvetkovic L. (2012) Texture and composition of Pb-bearing pyrite from the Coka Marin polymetallic deposit, Serbia, controlled by nanoscale inclusions. Can. Mineral. **50**, 1–20.

Palenik C S., Utsunomiya S., Reich M., Kesler S.E., Ewing R.C. (2004) "Invisible" gold revealed: direct imaging of gold nanoparticles in a Carlin-type deposit. Am. Mineral. **89**, 1359–1366.

Pérez-Flores, P., Cembrano, J., Sánchez-Alfaro, P., Veloso, E., Arancibia, G., Roquer, T.

(2016) Tectonics, magmatism and paleo-fluid distribution in a strike-slip setting: insights from the northern termination of the Liquiñe–Ofqui Fault System, Chile. Tectonophysics **680**, 192–210.

Peterson E.C. and Mavrogenes J.A. (2014) Linking high-grade gold mineralisation to earthquake-induced fault-valve processes in the Porgera gold deposit, Papua New Guinea. Geology **42**, 5, 383–386.

Piña R., Gervilla F., Barnes S.J., Ortega L., and Lunar R. (2013) Platinum-group elements-bearing pyrite from the Aguablanca Ni-Cu sulphide deposit (SW Spain): A LA-ICP-MS study. Eur. J. Mineral. **25**, 241–252.

Pokrovski G.S., Zakirov I.V., Roux J., Testemale D., Hazemann J.L., Bychkov A.V. and Golikova G. V. (2002) Experimental study of arsenic speciation in vapor phase to 500 °C: implications for As transport and fractionation in low-density crustal fluids and volcanic gases. Geochim. Cosmochim. Acta **66**, 3453–3480.

Pokrovski G.S., Roux J. and Harrichoury J.C. (2005) Fluid density control on vapor–liquid partitioning of metals in hydrothermal systems. Geology **33**, 657–660.

Pokrovski G.S., Borisova A.Y. & Bychkov A.Y. (2013) Speciation and transport of metals and metalloids in geological vapors. Rev. Mineral. Geochem. **76**, 165–218.

Pudack C., Halter W. E., Heinrich C. A., and Pettke T. (2009) Evolution of Magmatic Vapor to Gold-Rich Epithermal Liquid: The Porphyry to Epithermal Transition at Nevados de Famatina, Northwest Argentina. Econ. Geol. **104**, 449-477.

Qian G., Brugger J., Testamale D., Skiner W., and Pring A. (2012) Formation of As(II)-pyrite during experimental replacement of magnetite under hydrothermal conditions. Geochim.Cosmochim. Acta **100**, 1–10.

Radcliffe D. & McSween H.Y. (1969) Copper zoning in pyrite from Cerro de Pasco, Peru: a discussion. Am. Mineral. **54**, 1216-1217.

Reich M., Kesler S.E., Utsunomiya S., Palenik C.S., Chryssoulis S., and Ewing R.C. (2005) Solubility of gold in arsenian pyrite. Geochim.Cosmochim. Acta **69**, 2781–2796.

880 Reich M., Utsunomiya S., Kesler S.E., Wang L.M., Ewing R.C., and Becker U. (2006)
881 Thermal behavior of metal nanoparticles in geologic materials: Geology **34**, 1033–1036.

882 Reich, M., Chryssoulis, S.L., Deditius, A., Palacios, C., Zúñiga, A., Weldt, M., and
883 Alvear, M., 2010. "Invisible" silver and gold in supergene digenite (CuS). Geochim.
884 Cosmochim. Acta **74**, 6157–6173.

885 Reich M., Hough R., Deditius A., Utsunomiya S., Ciobanu C., and Cook N.J. (2011)
886 Nanogeoscience in ore systems research: Principles, methods and applications. Ore
887 Geol. Rev. **42**, 1–5.

888 Reich M., Deditius A., Chryssoulis S., Li J.W., Ma C.Q., Parada M.A., Barra F., and
889 Mittermayr F. (2013) Pyrite as a record of hydrothermal fluid evolution in a porphyry
890 copper system: A SIMS/EMPA trace element study. Geochim. Cosmochim. Acta **104**, p.
891 42–62.

892 Reich M., Simon A., Deditius A., Barra F., Chryssoulis S., Lagas G., Tardani D.,
893 Knipping J., Bilenker L.,, Sánchez-Alfaro P., Roberts M.P. and Munizaga R. (2016a).
894 Trace elemnt signature of pyrite from the Los Colorados Iron Oxide-Apatite (IOA)
895 deposit, Chile: a missing link between Andean IOA and Iron Oxide Copper-Gold
896 systems? Econ. Geol **111**, pp. 743–761.

897 Reich M., Large R., Deditius A. (2016b) New advances in trace element geochemistry
898 of ore minerals and accessory phases. Ore Geol. Reviews (in press),
899 http://dx.doi.org/10.1016/j.oregeorev.2016.10.020.

900 Rosenau M., Melnick D., Echtler H. (2006) Kinematic constraints on intra-arc shear and
901 strain partitioning in the southern Andes between 38°S and 42°S latitude. Tectonics **25**,
902 1–16. doi:10.1029/2005TC001943.

903 Rusk B.G., Reed M.H. and Dilles J.H. (2008) Fluid inclusion evidence for magmatic-
904 hydrothermal fluid evolution in the porphyry copper–molybdenum deposit at Butte,
905 Montana. Econ. Geol. **103**, 307–334.

906 Sánchez P., Pérez-Flores P., Arancibia G., Cembrano J., Reich M. (2013) Crustal
907 deformation effects on the chemical evolution of geothermal systems: the intra-arc

908 Liquiñe–Ofqui fault system, Southern Andes. Int. Geol. Rev. **55**, 1384–1400. 939
909 doi:10.1080/00206814.2013.775731

910 Sánchez-Alfaro P., Reich M., Arancibia G., Pérez-Flores P., Cembrano J., Driesner T.,
911 Lizama M. Rowland J., Morata D., Heinrich C. A., Tardani D., Campos E. (2016a)
912 Physical, chemical and mineralogical evolution of the Tolhuaca geothermal system,
913 southern Andes, Chile: insights into the interplay between hydrothermal alteration and
914 brittle deformation. J.Volcanol. Geoth. Res. **324**, 88–104.

915 Sánchez-Alfaro P., Reich M., Driesner T., Cembrano J., Arancibia G., Pérez-Flores P.,
916 Heinrich C. A., Rowland J., Tardani D., Lange D., Campos E. (2016b) The optimal
917 windows for seismically-enhanced gold precipitation in the epithermal environment.
918 Ore Geol. Rev. **79**, 463–473

919 Saunders J.A. (1990) Colloidal transport of gold and silica in epithermal precious-metal
920 systems: evidence from the Sleeper deposit, Nevada. Geology **18**, 757–760.

921 Schmid-Beurmann P. and Bente K. (1995): Stability properties of the CuS2–FeS2 solid
922 solution series of pyrite type. Mineral. Petrol. **53**, 333-341.

923 Shimazaki H. & Clark L.A. (1970) Synthetic FeS2–CuS2 solid solution and fukuchilite-
924 like minerals. Can. Mineral. **10**, 648-664.

925 Shoji T., Iwano H., Kaneda H., Takenouchi S. (1989) Trace elements in pyrite from
926 Kirishima geothermal field and their availability for exploration. J. Geotherm. Res. Soc.
927 Jpn. **11**, 31–42.

928 Shoji T., Kaneda H., Takano Y. (1999) Minor element geochemistry in the Yanaizu-
929 Nishiyama geothermal field, Northeastern Japan. Geotherm. Resour. Counc. Trans. **23**,
930 405–406.

931 Simmons S.F., Browne P.R.L. (2000) Hydrothermal minerals and precious metals in the
932 Broadlands-Ohaaki geothermal system: implications for understanding low sulfidation
933 epithermal environments. Econ. Geol. **95**, 971–999.

934 Simmons S.F., Browne K.L., Browne P.R.L, Rowland J.V. (2016a) Gold and silver
935 resources in Taupo Volcanic Zone geothermal systems. Geothermics **59**, 205–214.

936 Simmons S.F., Brown K.L., Tutolo B.M. (2016b) Hydrothermal Transport of Ag, Au,
937 Cu, Pb, Te, Zn, and Other Metals and Metalloids in New Zealand Geothermal Systems:
938 Spatial Patterns, Fluid-Mineral Equilibria, and Implications for Epithermal
939 Mineralization. Econ. Geol. **111**, 589–618.

940 Simon G., Huang H., Penner-Hahn J.E., Kesler S.E. and Kao L.S. (1999) Oxidation
941 state of gold and arsenic in gold-bearing arsenian pyrite. Am. Miner. **84**, 1071–1079.

942 Simon A.C., Pettke T., Candela P.A., Piccoli P.M., and Heinrich C.A. (2006) Cu
943 partitioning in a melt-vapor-brine-magnetite-pyrrhotite assemblage. Geochim.
944 Cosmochim. Acta **70**, 5583–5600.

945 Simon A. C., Pettke T., Candela P. A., Piccoli P. M., and Heinrich C. A. (2007) The
946 partitioning behavior of As and Au in S-free and S-bearing magmatic assemblages.
947 Geochim. Cosmochim. Acta, **71**, 1764–1782.

948 Skinner B. J., White D. E., Rose H. J., Mays R. E. (1967) Sulfides associated with the
949 Salton Sea geothermal brine. Econ. Geol. **62**, 316–330.

950 Soltani Dehnavi A., Lentz D. R., and McFarlane C. R. M. (2015) LA-ICPMS analysis
951 of volatile trace elements in massive sulphides and host rocks of selected VMS deposits
952 of the Bathurst mining camp, New Brunswick: Methodology and application to
953 exploration. Geological Survey of Canada Open File 7853, 214.

954 Steadman, J. A., Large, R. R., Meffre, S., Olin, P. H., Danyushevsky, L. V., Gregory, D.
955 D., Belousov, I., Lounejeva, E., Ireland, T. R., and Holden, P. (2015) Synsedimentary to
956 Early Diagenetic Gold in Black Shale-Hosted Pyrite Nodules at the Golden Mile
957 Deposit, Kalgoorlie, Western Australia. Econ. Geol. **110**, 5, 1157-1191.

958 Sung Y. H., Brugger J., Ciobanu C. L., Pring A., Skinner W. and Nugus M. (2009)
959 Invisible gold in arsenian pyrite and arsenopyrite from a multistage Archean gold
960 deposit: sunrise Dam Eastern Goldfields Province, Western Australia. Miner. Deposita
961 **44**, 765–791.

962 Tanner D., Henley R. W., Mavrogenes J.A., Holden P. (2016) Sulfur isotope and trace
963 element systematics of zoned pyrite crystals from the El Indio Au–Cu–Ag deposit,

964 Chile. Contr. Mineral. Pet. **171** (4), 1-17

965 Tardani D., Reich M., Roulleau E., Takahata N., Sano Y., Pérez-Flores P., Sánchez-
966 Alfaro P., Cembrano J., Arancibia G. (2016). Exploring the structural controls on
967 helium, nitrogen and carbon isotope signatures in hydrothermal fluids along an intra-arc
968 fault system. Geochim. Cosmochim. Acta **184**, 193–211.

969 Thiele R., Lahsen A., Hugo M., Varela J., Munizaga F. (1987) Estudio geológico
970 regional a escala 1:100.000 de la Hoya Superior y Curso Medio del Río Bío-Bío.
971 Centrales Quitramán, Huequecura, Aguas Blancas, Pangue, Ralco y Llanquén. Depto.
972 de Geología-ENDESA (In spanish).

973 Tossell J. A., Vaughan D. J., Burdett J. K. (1981) Pyrite, marcasite, and arsenopyrite-
974 type minerals: crystal chemical and structural principles. Phys. Chem. Miner. **7**, 177–
975 184.

976 Vaughan D. J., Craig J. R. (1978) Mineral Chemistry of Metal Sulfides. Cambridge
977 Univ. Press, Cambridge.

978 Vaughan J. P. and Kyin A. (2004) Refractory gold ores in Archean greenstones, Western
979 Australia: mineralogy, gold paragenesis, metallurgical characterization and
980 classification. Mineral. Mag. **68**, 255–277.

981 Wilkinson, J. J., Stoffell, B., Wilkinson, C. C., Jeffries, T. E., and Appold, M. S. (2009)
982 Anomalously metal-rich fluids form hydrothermal ore deposits. Science **323**, 764-767.

983 Williams-Jones A. E., and Heinrich C. A. (2005) Vapor transport of metals and the
984 formation of magmatic-hydrothermal ore deposits. Economic Geology 100th
985 Anniversary Volume 1905–2005 **100**, 1287–1312.

986 Williams-Jones A. E., Migdisov A. A., Archibald S. M., and Xiao Z. (2002) Vapor
987 transport of ore metals, in Hellmann, R., and Wood, S.A., eds., Water-rock interactions,
988 ore deposits, and environmental geochemistry. A tribute to David A. Crerar.
989 Geochemical Society Special Publication **7**, 279–305.

990 Zajacz Z., Halter W. (2009) Copper transport by high temperature, sulfur-rich magmatic
991 vapor: Evidence from silicate melt and vapor inclusions in a basaltic andesite from the

Villarrica volcano (Chile). Earth Planet. Sci. Lett. **282**, 115–121.

Zajacz Z. (2007) Mass transfer during volatile exsolution in magmatic systems: Insights through methodological developments in melts and fluid inclusion analysis [Ph.D. thesis]. ETH Zürich Monograf 17448, 169.

Zajacz Z., Seo J. H., Candela P. A., Piccoli P. M. and Tossell J. A. (2011) The solubility of copper in high-temperature magmatic vapors: A quest for the significance of various chloride and sulfide complexes. Geochim. Cosmochim. Acta **75**, 2811–2827.

FIGURE CAPTIONS

Figure 1. Geological map of the Tolhuaca Geothermal System (TGS), modified from Aravena et al. (2016) and Sánchez-Alfaro et al. (2016a). The main geologic units, structures, surface thermal features and geothermal well locations, as well as the schematic cross section, were modified from Sánchez-Alfaro et al. (2016a). Simplified lithology of the Tol-1 well and hydrothermal alteration zones were taken from Melosh et al. (2010; 2012) and Sánchez et al. (2013). Depth location is indicated for pyrite-bearing samples PFI-2, PFI-3, PFI-26, PFI-39, PFI-41 and PFI-45. LOFZ: Liquiñe Ofqui Fault Zone; ALFS: Arc-oblique Long-lived Basement Fault System.

Figure 2. Backscattered electron (BSE) images showing representative textural relationships of pyrite-bearing samples from the TGS. Pyrite occurs as disseminated grains (A, B, C, E, F) and in silica veinlets (C, D), and is mainly associated with Fe-oxide (A) and chalcopyrite (E). Chalcopyrite inclusions in pyrite are visible in selected grains (F). Py: pyrite; FeOx: Fe-oxide; Zeo: zeolite; Ab: albite, Cpy: chalcopyrite. The red line (F) shows an EMPA traverse (see table 1, sample PFI-39, datapoints 44a T3).

Figure 3. Concentration plot for minor and trace elements in pyrite (samples PF-2, PF-3, PF-26, PF-39, PF-41 and PF-45). Pyrite data from argillic and propylitic alteration zones are identified by black circles and open squares, respectively. Data are plotted in parts per million (ppm) on a vertical logarithmic scale. For each element, median concentrations measured by EPMA (solid lines) and SIMS (segmented lines) are shown

1023 together with maximum and minimum values. Outliers are shown as red crosses. The
1024 horizontal dotted line is the mean detection limit (mdl) of EPMA analysis for all
1025 elements (~100 ppm).
1026
1027 **Figure 4.** Representative microtextures and chemical zonations of pyrite from the
1028 (shallow) argillic alteration zone of the Tolhuaca Geothermal System. Samples: PFI-2
1029 (a, b, c, d, e, f and g) and PFI-3 (h, i, j, k, l, m, n, o, p and q). (a), (e) and (h):
1030 backscattered electron (BSE) image showing pyrite (Py) crystals. (b), (c), and (d):
1031 quantitative wavelength dispersive spectrometry (WDS) X-ray maps of area in (a) for
1032 As (Kα), Co (Kα), and Cu (Kα), respectively. (f) and (g) show WDX maps of area in
1033 (e) for As (Lα) and Cu (Kα), respectively. (i), (j) and (k) show WDX maps of area in
1034 (h) for As (Lα), Co (Kα), and Cu (Kα), respectively. (l) and (o); (m) and (p); and (n)
1035 and (q) show WDX maps of disseminated pyrite grains for As (Lα), Co (Kα), and Cu
1036 (Kα), respectively. Quantitative WDX maps for As (Lα) Co (Kα), and Cu (Kα) show
1037 zonations of these metals. Cu (Kα) distributions in (d), (k) and (n) show discrete
1038 inclusions of chalcopyrite. A color scale bar for concentration (in wt %) is shown for
1039 each WDS map. Py: pyrite.
1040
1041 **Figure 5.** Representative microtextures and chemical features of pyrite from the deep
1042 (propylitic) alteration zone. Samples: PFI-39 (a, b, c) and PFI-41 (d, e, f). (a) and (d)
1043 show quantitativeWDX maps for As. (b) and (e) show maps for Co (Kα). (c) and (f)
1044 show WDX maps for Cu (Kα). Cu (Kα) distribution in (c) shows discrete inclusions of
1045 chalcopyrite. Color scale bars for concentration (in wt %) are shown. Py: pyrite.
1046
1047 **Figure 6.** Ternary diagram showing the As-Fe-S composition of pyrite in the Tolhuaca
1048 Geothermal System. Five different trends show substitution of (i) As for S (As^{1-} - pyrite;
1049 green arrow); (ii) As^0 nano-inclusions (As^0 red arrow); (iii) As^{2+} for Fe (As^{2+} -pyrite;
1050 light green arrow); (iv) As^{3+} for Fe (As^{3+}-pyrite; orange arrow); and (v) divalent metals
1051 Me^{2+} for Fe (blue arrow). The composition of As^{2+}-pyrite (after Qian et al., 2013;
1052 Deditius et al., 2014) was calculated based on the assumption of ideal occupancy of S
1053 (66.66 at.%). n = 2924.
1054

Figure 7. Elemental correlation plots of (a) As vs. S, (b) As vs. Fe, (c) Cu vs. Fe, (d) Cu vs. As, (e) Co vs. Fe, and (f) Co vs. Cu. Black diamonds, open diamonds, open squares, open triangles, black circles and open circles represents pyrite samples PFI-2, PFI-3, PFI, 26, PFI, 39, PFI, 41 and PFI-45, respectively. R^2 values are shown.

Figure 8. SIMS depth-concentration profiles (time vs. intensity) of trace elements in pyrite from Tolhuaca Geothermal System. Spiky profiles for ^{63}Cu (c and d) reflect the presence of individual nanoinclusions or clusters of mineral nanoparticles (colored circles and ovals), whereas ^{59}Co (a), ^{75}As (b), and ^{197}Au (e and f) show a more homogeneous (solid-solution) distribution. Major sulfide-matrix constituent isotopes, ^{56}Fe and ^{34}S, were monitored during each run (top). Vertical intensity scale is in counts per second (cps); horizontal (depth) scale is in micrometers (μm).

Figure 9. Elemental correlation plots of (a) Co vs. Ni, (b) Au vs. As, (c) Te vs. Au, (d) Ag vs. Au, (e) Ag vs. As and (f) Pb vs. Fe. Black diamonds, open diamonds, open squares, open triangles, black circles and open circles represents pyrite samples PFI-2, PFI-3, PFI, 26, PFI, 39, PFI, 41 and PFI-45, respectively. Solid lines in (a) represent Co/Ni=1 and Co/Ni=10. The curve in (b) is the As-dependent solubility of Au in pyrite as determined by Reich et al. (2005). R^2 values are shown.

Figure 10. SIMS depth-concentration profiles (time vs. intensity) of trace elements in pyrite from the TGS. Spiky profiles for ^{109}Ag (a and b), and ^{80}Se (e and f) reflect presence of individual nanoinclusions or clusters of mineral nanoparticles (colored circles and ovals), whereas ^{130}Te (c) and ^{123}Sb (d) show a more homogeneous (solid-solution) distribution. Major sulfide-matrix constituent isotopes, ^{56}Fe and ^{34}S, were monitored (top). Vertical intensity scale is in counts per second (cps); horizontal (depth) scale is in micrometers (μm).

Figure 11. Combination of pyrite data (WDS X-ray maps) with LA-ICP-MS analyses of fluid inclusions in pyrite-bearing veins and borehole fluids chemical data at the TGS, The panels (a) and (b) show a pyrite grain from the argillic zone that contains a Cu-rich, As-poor core (P1), and an As-rich, Cu-poor rim (P2). The panels (c) shows the Cu/As ratio of fluid inclusions (red circles) and borehole fluids samples (green circles), respectively, reported by Sánchez-Alfaro et al. (2016a). The Cu-rich, As-poor pyrite

1089 core (P1) correlates with the high Cu/As ratios measured in fluid inclusions in calcite-
1090 quartz-pyrite veins. Conversely, As-rich and Cu-poor pyrite rims (P2) correlate with the
1091 low Cu/As and ratio measured in the present-day borehole fluid.
1092

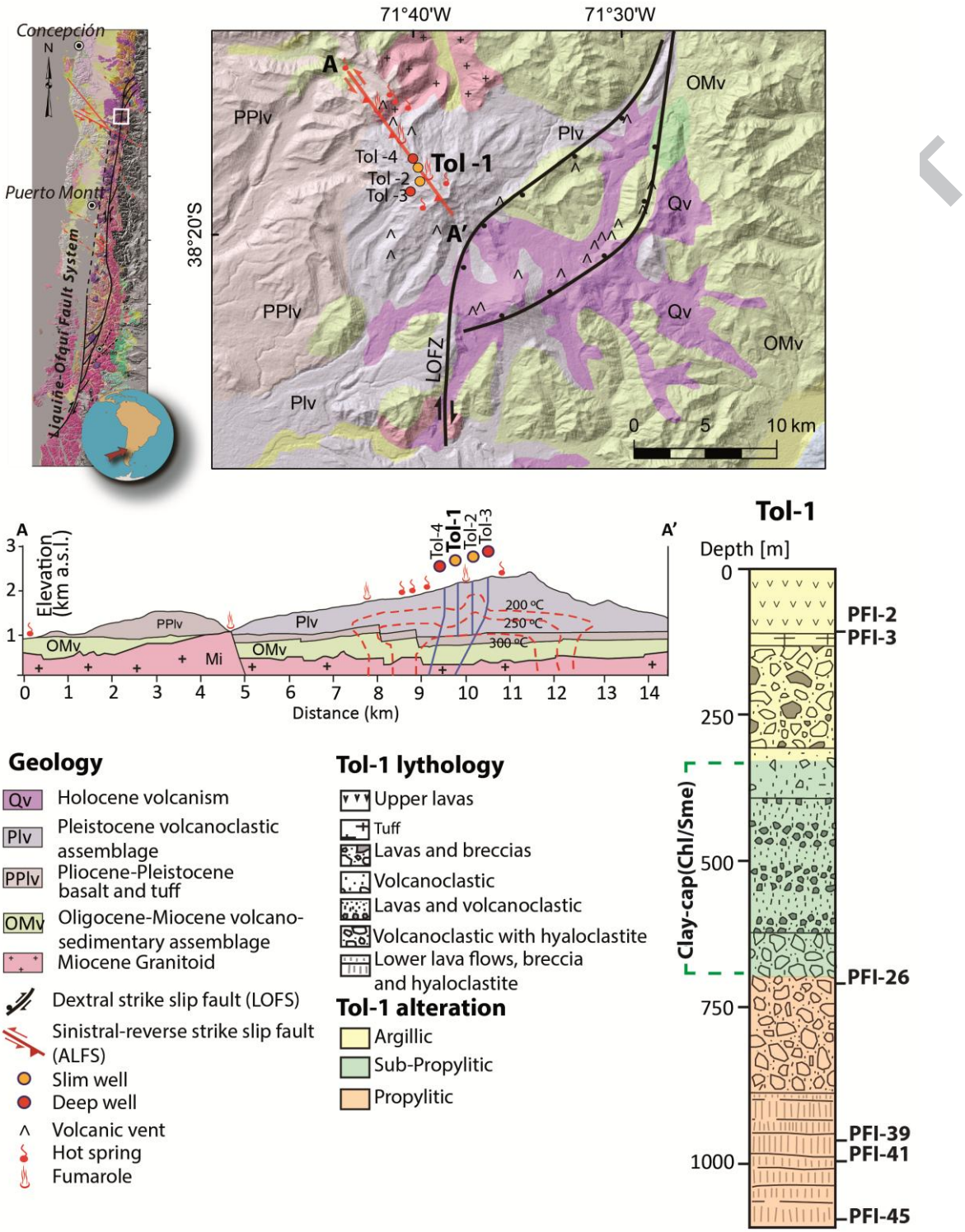

1093

1094

1095

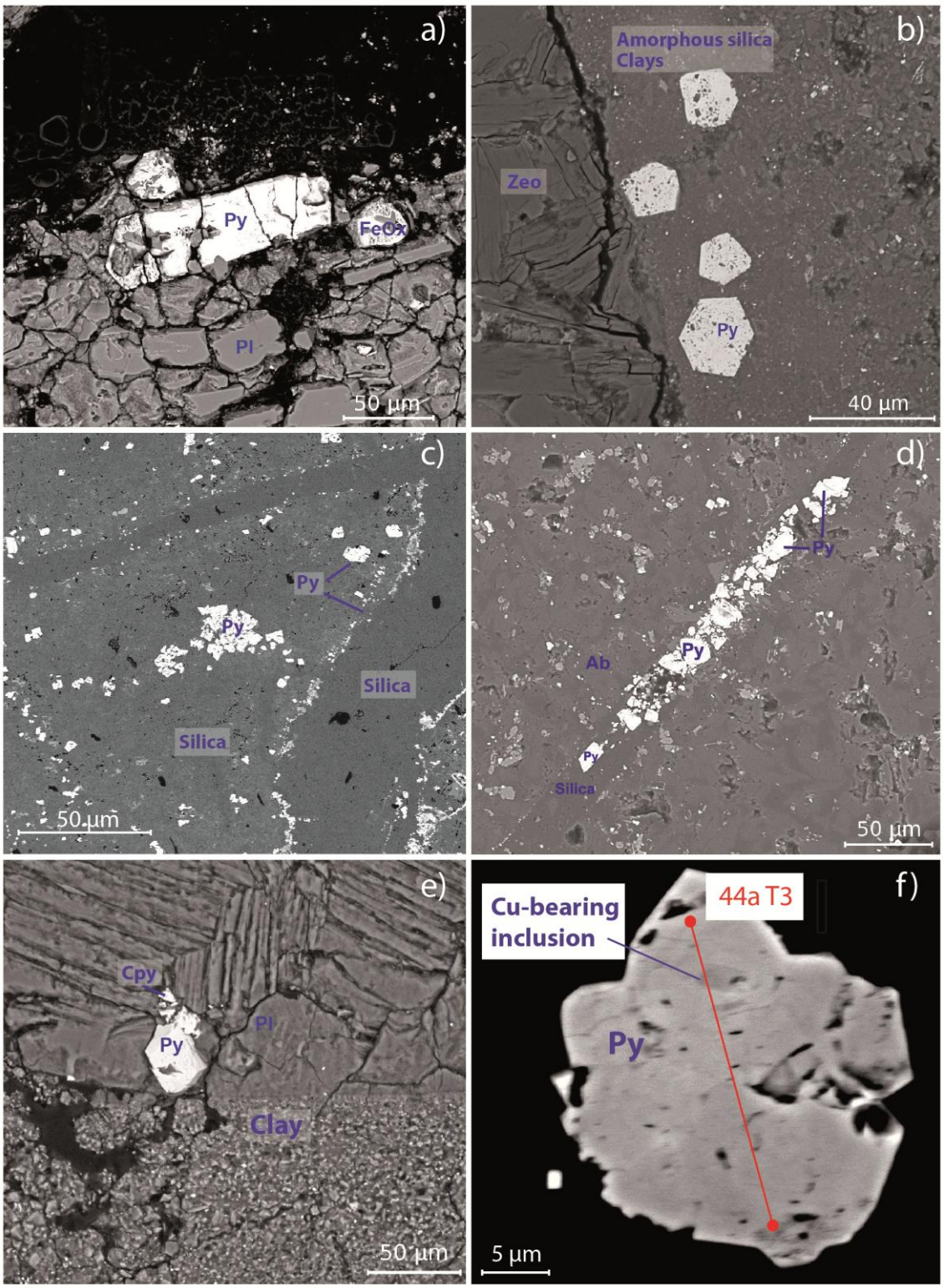

1096

1097

1098

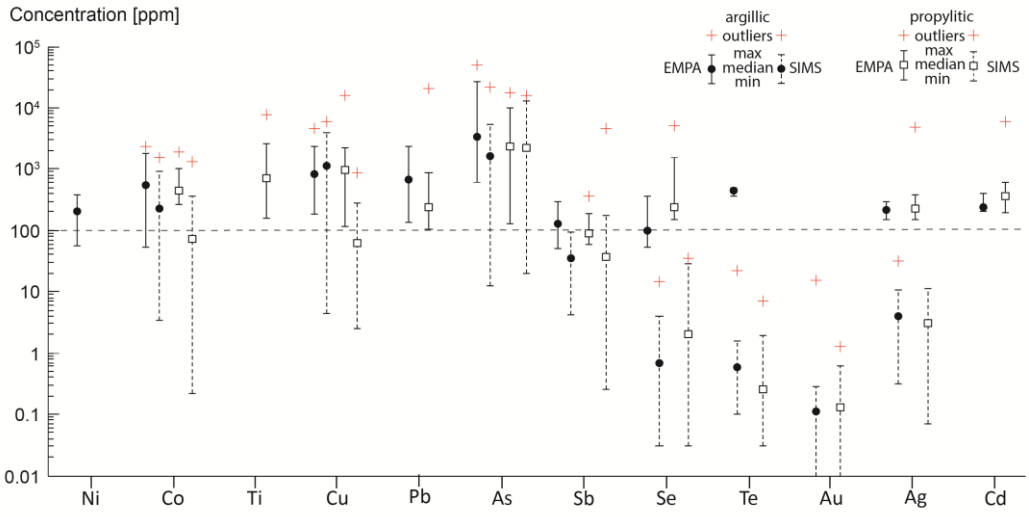

1099

1100

1101

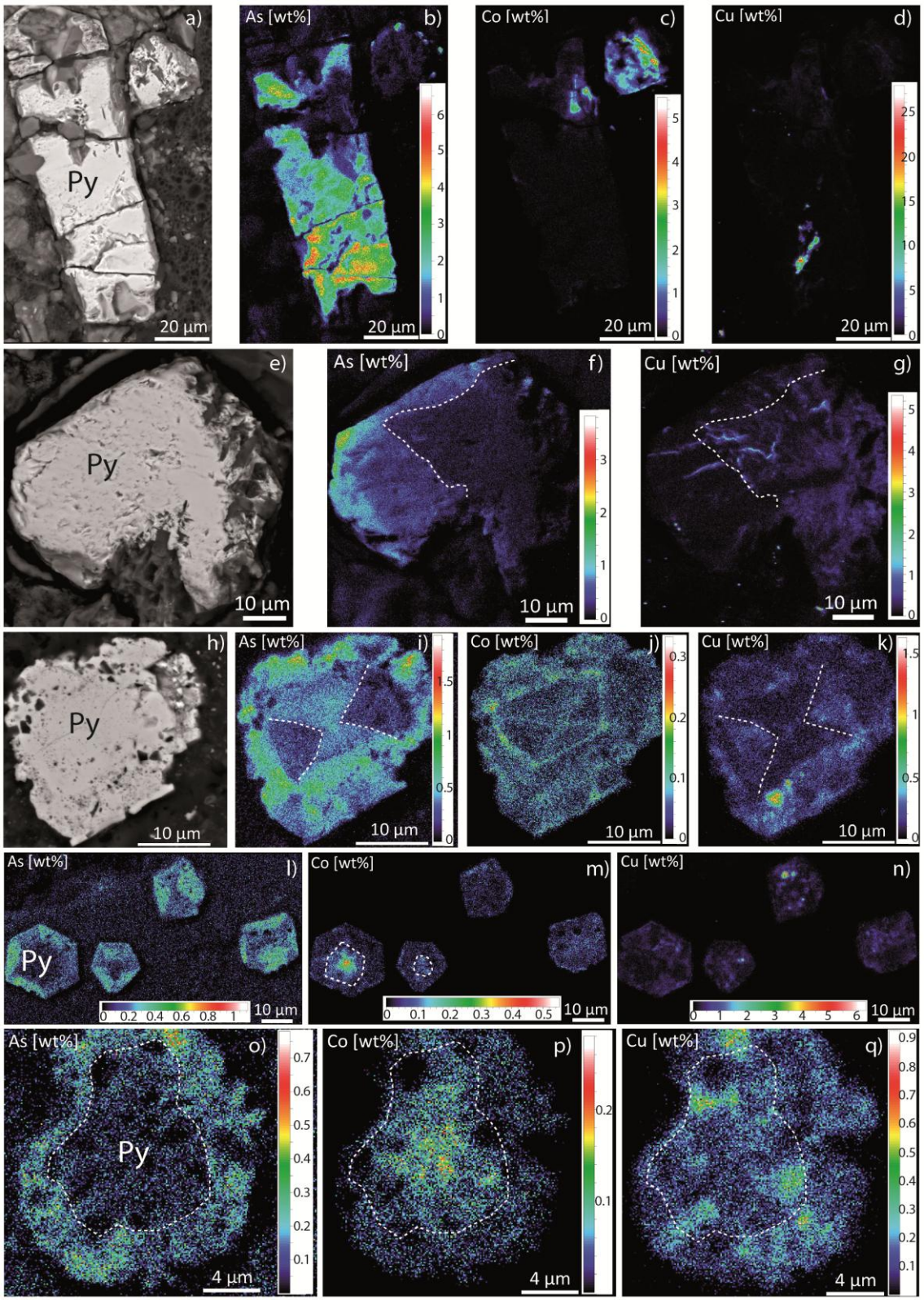

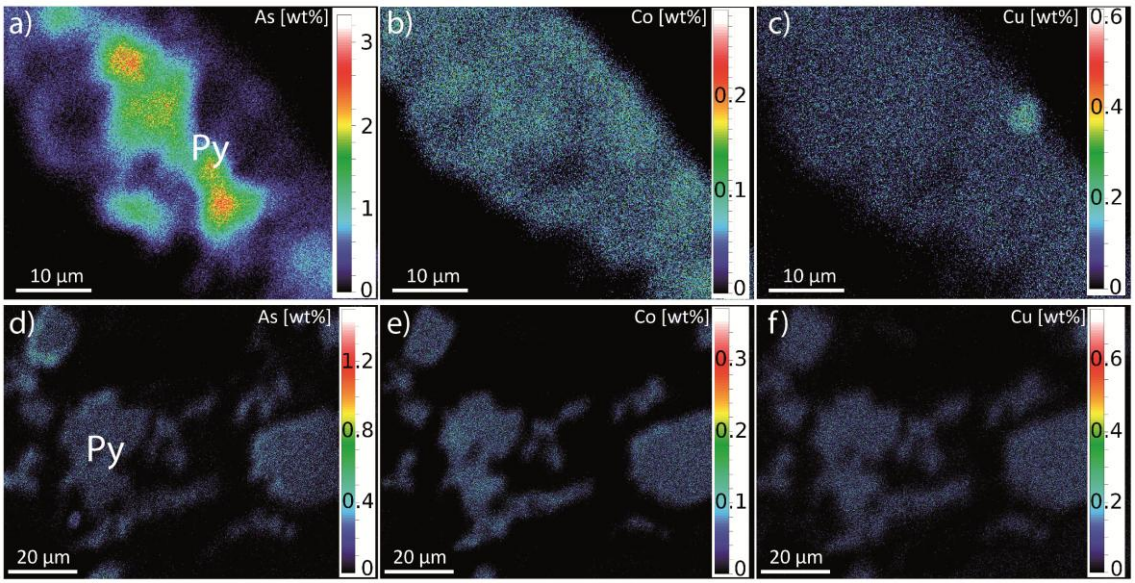

1105

1106

1107

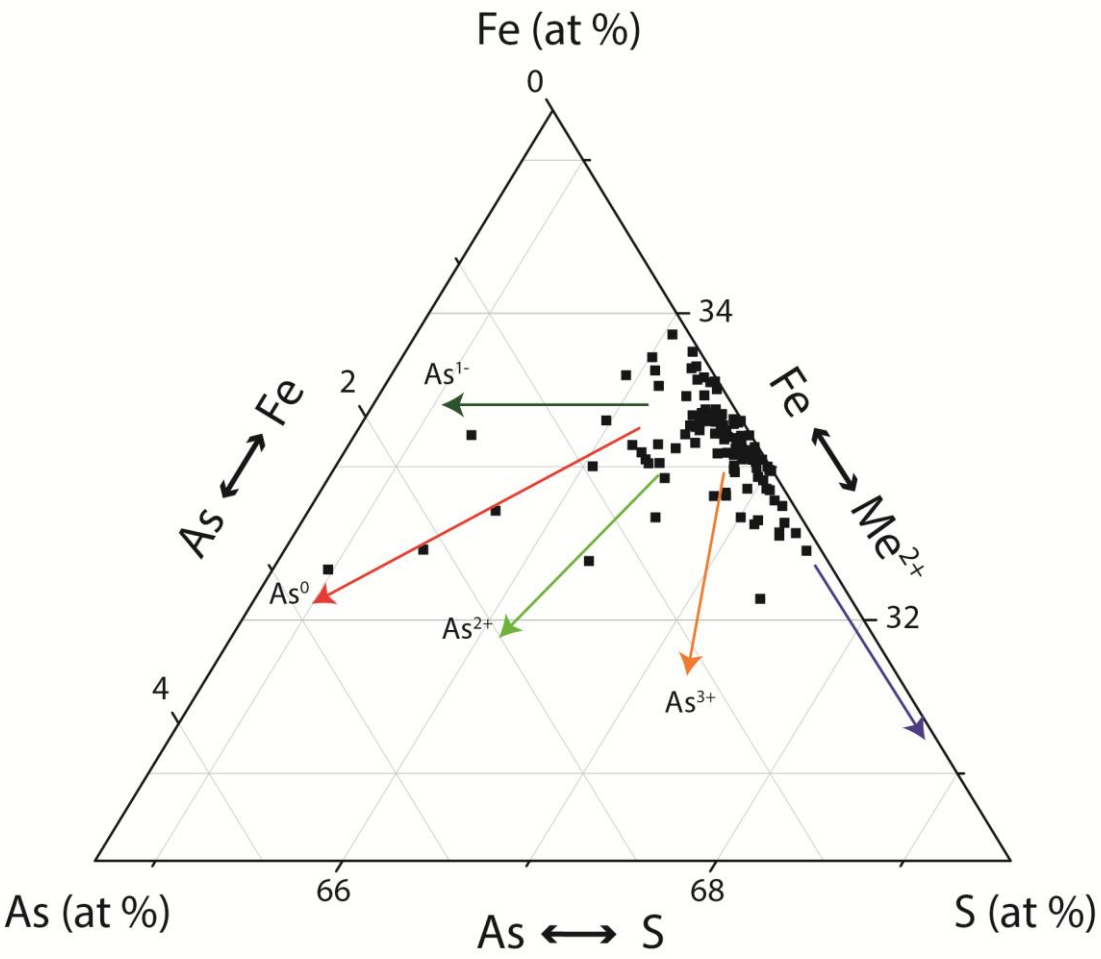

1108

1109

1110

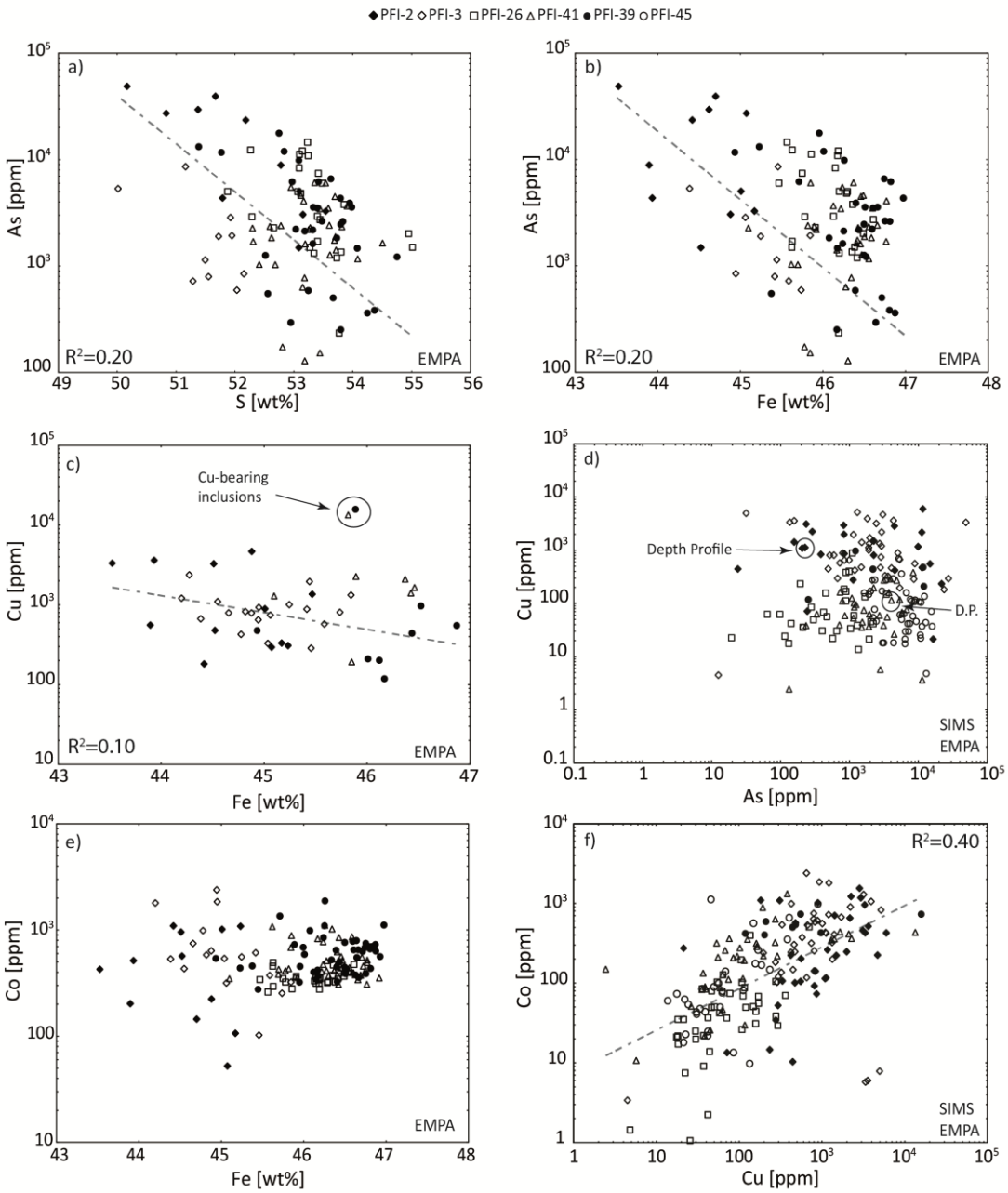

1111

1112

1113

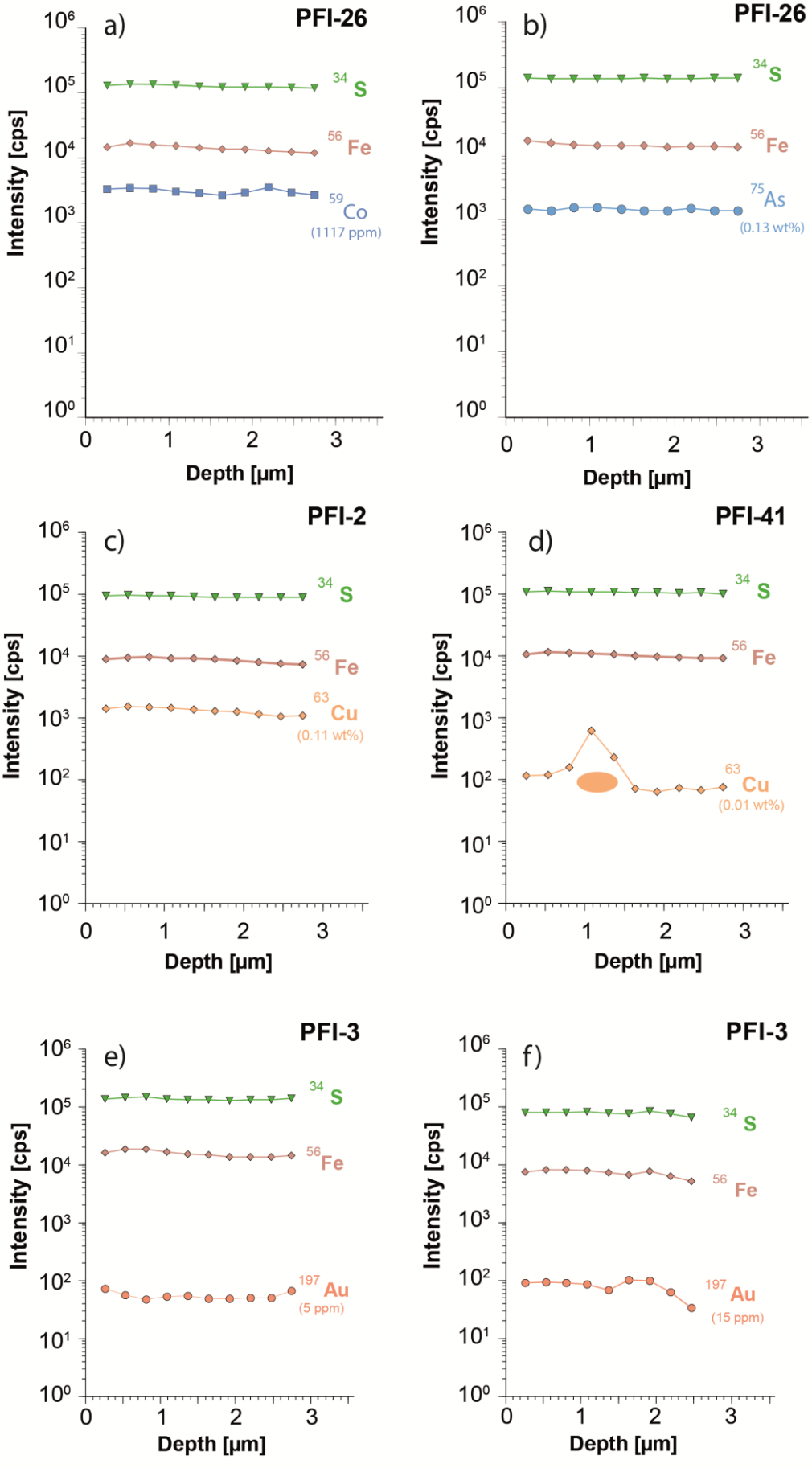

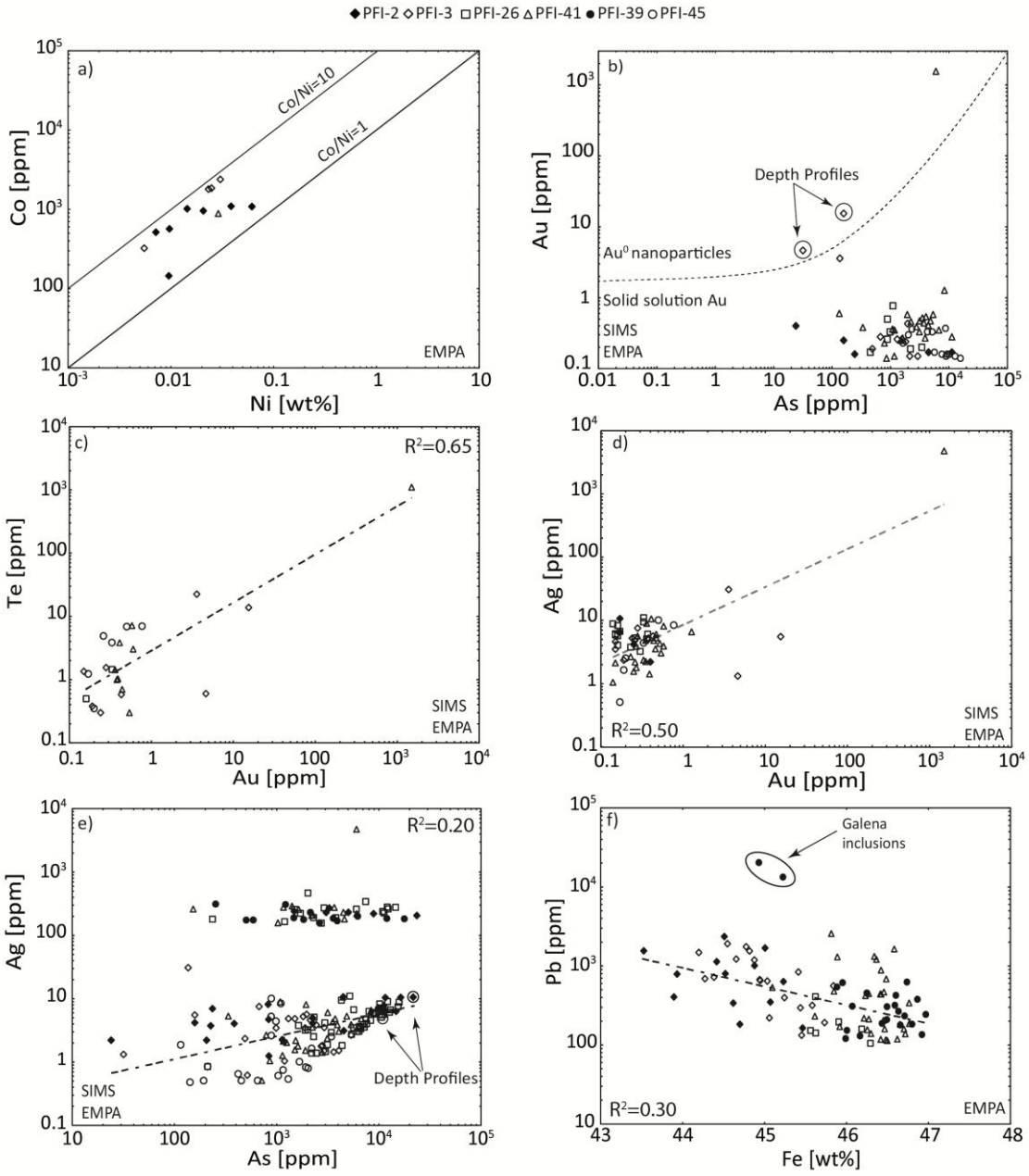

1115

1116

1117

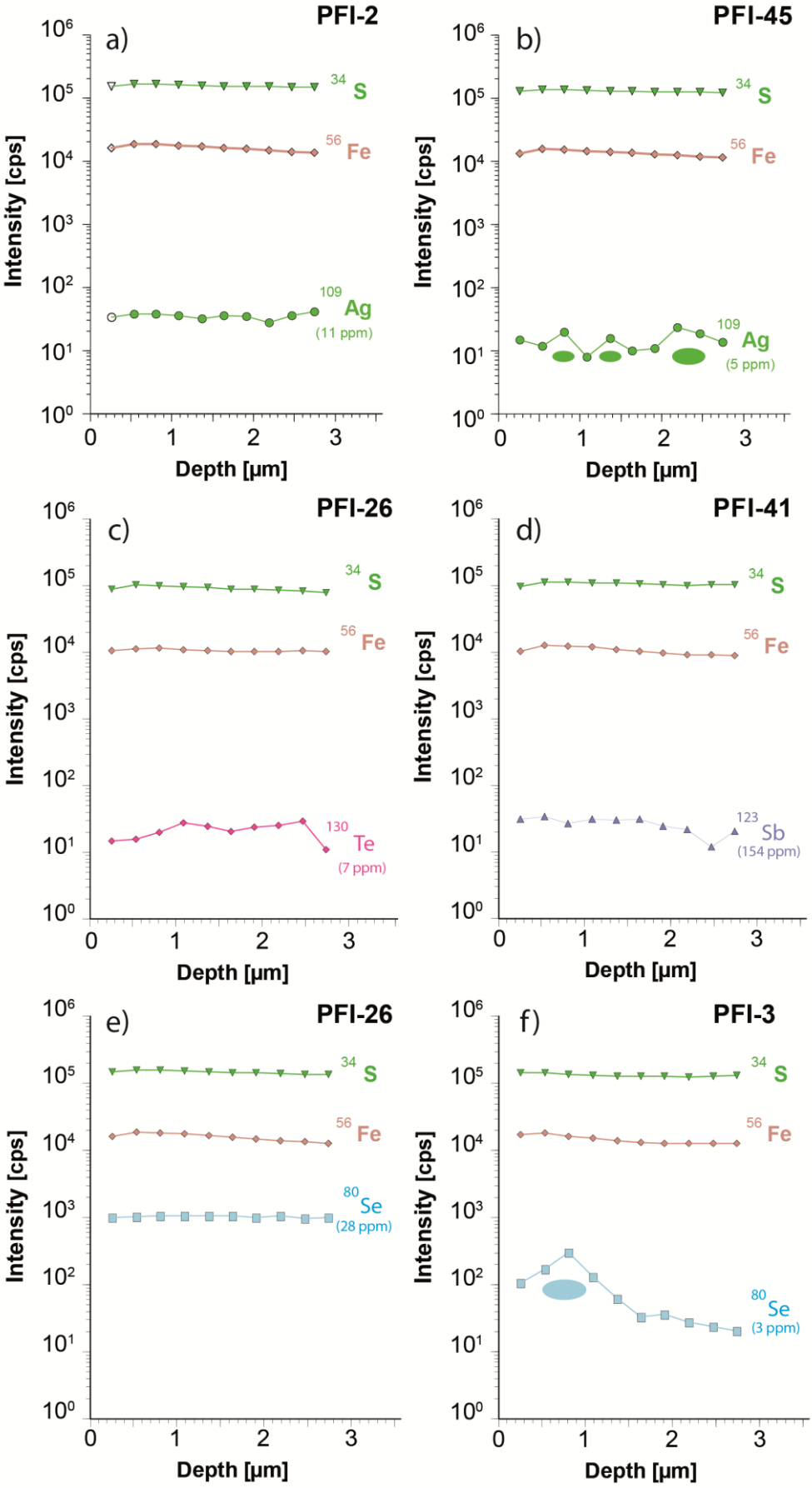

1119

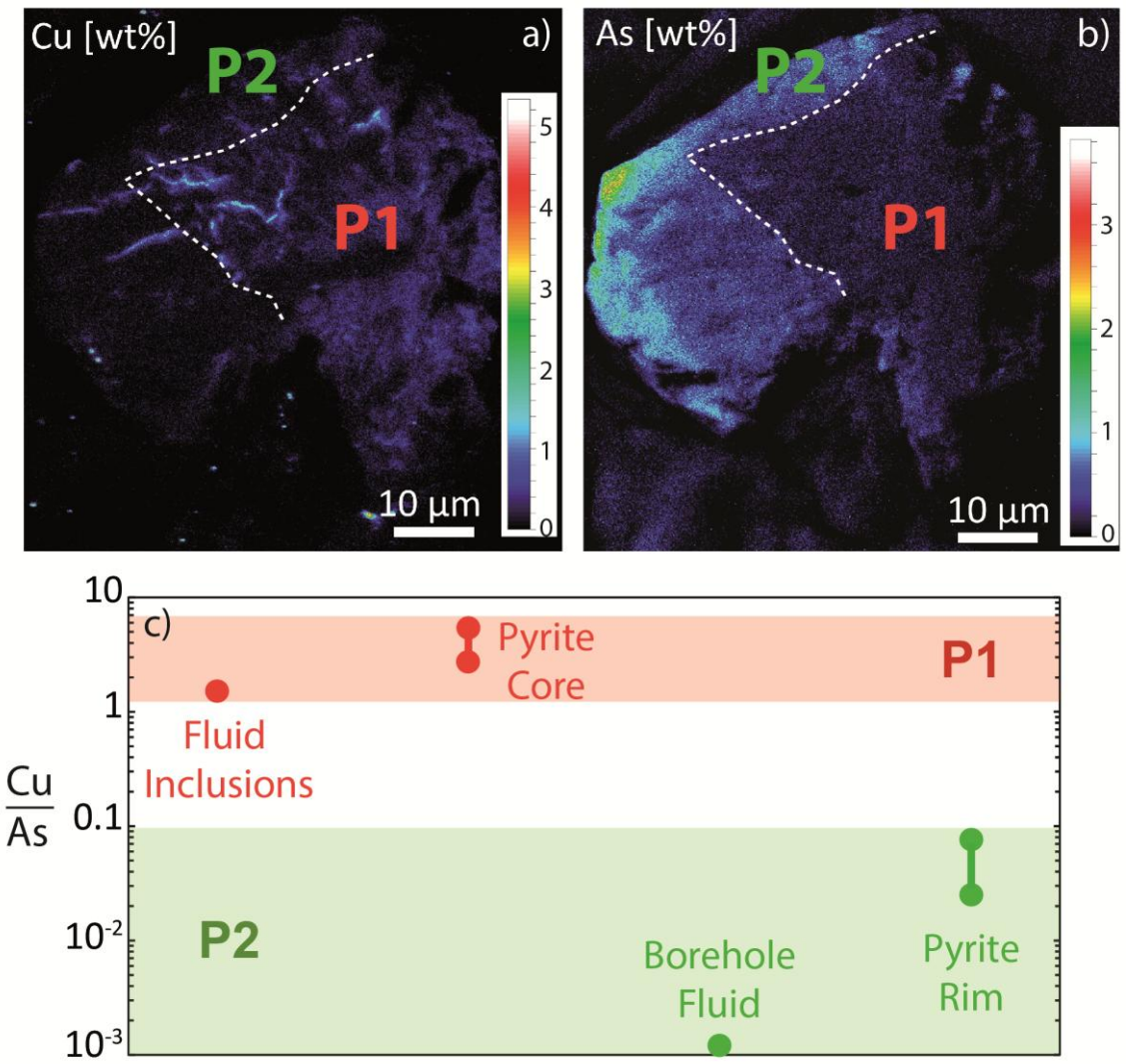

1120

1121

1122

Table 4.1. *Representative EPMA Analyses (wt %) of Pyrite from the Tolhuaca Geothermal System. Py: pyrite, Cpy: chalcopyrite, Br: bornite.*

SAMPLE	S WT %	Fe WT %	Co WT %	Cu WT %	Ni WT %	Pb WT %	Ti WT %	As WT %	Sb WT %	Se WT %	Te WT %	Au WT %	Ag WT %	Cd WT %	TOTAL
PFI-2															
p1-1	50.83	45.07	0.01	0.03	n.d.	0.03	n.d.	2.72	0.01	n.d.	n.d.	n.d.	n.d.	n.d.	98.75
p1-2	51.67	44.70	0.01	n.d.	0.01	0.02	n.d.	3.93	0.02	0.01	n.d.	n.d.	n.d.	0.03	100.47
p3-1	52.18	44.42	0.11	0.02	0.04	0.11	n.d.	2.35	0.01	0.01	n.d.	n.d.	0.02	0.03	99.30
p2-1	51.37	44.62	n.d.	n.d.	n.d.	0.03	n.d.	2.95	0.01	n.d.	n.d.	n.d.	n.d.	n.d.	99.09
p5-1	53.16	44.51	0.10	0.33	0.02	0.24	n.d.	n.d.	0.01	n.d.	n.d.	n.d.	0.03	0.04	98.43
p4-1	53.16	44.88	0.02	0.47	n.d.	0.10	n.d.	0.30	n.d.	n.d.	n.d.	n.d.	0.02	n.d.	98.99
p8-1	53.09	45.01	0.10	0.09	0.01	0.17	n.d.	0.50	0.02	0.03	n.d.	n.d.	0.02	n.d.	99.13
p8-2	51.79	43.93	0.05	0.36	0.01	0.08	n.d.	0.43	n.d.	n.d.	n.d.	n.d.	n.d.	0.02	96.70
p8-3	53.09	44.52	0.06	0.05	0.01	0.08	n.d.	0.15	n.d.	n.d.	n.d.	n.d.	0.02	0.02	98.02
p8-4	52.78	43.90	0.02	0.06	n.d.	0.04	n.d.	0.89	n.d.	n.d.	n.d.	n.d.	0.02	0.04	97.75
p7-1	50.01	45.23	0.11	0.03	0.06	0.06	n.d.	n.d.	0.01	n.d.	0.04	n.d.	n.d.	n.d.	95.60
p7-2	52.79	45.47	n.d.	0.14	n.d.	0.02	n.d.	n.d.	0.01	n.d.	0.05	n.d.	n.d.	n.d.	98.58
p7-3	53.54	45.17	0.01	0.03	n.d.	n.d.	n.d.	0.33	n.d.	n.d.	n.d.	n.d.	0.03	0.02	99.13
p6	50	43.	0.0	0.3	n.d	0.1	n.	4.8	0.0	0.0	0.0	n.d	n.d	n.d	99.

-1	.17	53	4	3	.	6	d.	8	3	4	4	.	.	.	26
PFI-3															
p3-1	52.76	44.82	0.06	0.08	n.d.	0.15	n.d.	n.d.	0.01	0.01	n.d.	n.d.	n.d.	n.d.	97.92
p3-4	51.67	44.27	n.d.	0.24	n.d.	0.07	n.d.	n.d.	0.01	n.d.	n.d.	n.d.	n.d.	0.02	96.31
p4-1	52.15	44.94	0.24	0.06	0.03	0.07	n.d.	0.08	0.02	n.d.	n.d.	n.d.	0.02	n.d.	97.67
p4-2	52.07	44.88	0.06	0.08	n.d.	0.12	n.d.	n.d.	0.01	n.d.	n.d.	n.d.	n.d.	0.02	97.29
p4-3	51.46	44.55	0.04	0.11	n.d.	0.19	n.d.	n.d.	0.01	n.d.	n.d.	n.d.	0.02	n.d.	96.43
p4-4	51.74	45.04	0.05	0.03	n.d.	0.06	n.d.	n.d.	0.01	n.d.	n.d.	n.d.	n.d.	n.d.	96.98
p4-5	51.27	44.20	0.18	0.12	0.02	0.15	n.d.	n.d.	0.02	n.d.	n.d.	n.d.	0.02	n.d.	96.04
p1-2	51.60	44.95	0.18	0.09	0.02	0.07	n.d.	n.d.	0.01	n.d.	n.d.	n.d.	0.02	n.d.	96.97
p1-4	51.95	45.84	0.03	0.13	0.01	0.06	n.d.	0.19	0.01	n.d.	n.d.	n.d.	n.d.	n.d.	98.26
p1-5	51.16	45.46	0.01	0.03	n.d.	0.01	n.d.	0.86	0.02	n.d.	n.d.	n.d.	n.d.	n.d.	97.58
p2-4	51.29	45.59	0.04	0.06	n.d.	0.03	n.d.	0.07	0.02	n.d.	n.d.	n.d.	n.d.	n.d.	97.12
p2-5	52.03	45.74	0.03	0.08	n.d.	0.02	n.d.	0.06	0.01	n.d.	n.d.	n.d.	n.d.	n.d.	98.00
p2-7	51.08	44.78	0.10	0.04	n.d.	0.17	n.d.	n.d.	0.01	n.d.	n.d.	n.d.	n.d.	n.d.	96.20
p2-8	51.72	45.25	0.06	0.10	n.d.	0.04	n.d.	0.19	0.02	n.d.	n.d.	n.d.	n.d.	n.d.	97.43
p5-2	51.55	45.42	0.06	0.09	n.d.	0.08	n.d.	0.08	0.01	n.d.	0.05	n.d.	n.d.	n.d.	97.38
p5	51	44.	0.0	0.0	n.d	0.1	n.	n.d	0.0	n.d	n.d	n.d	0.0	n.d	96.

-5	.79	66	7	8	.	2	d.	.	1	.	.	.	2	.	82
p7-1	50.01	44.39	0.05	0.07	n.d.	0.07	n.d.	0.53	0.02	0.01	n.d.	n.d.	n.d.	n.d.	95.17
p7-4	51.49	45.44	n.d.	0.20	n.d.	0.03	n.d.	0.11	0.02	n.d.	n.d.	n.d.	n.d.	n.d.	97.33
p7-5	51.93	45.06	0.03	0.07	n.d.	0.02	n.d.	0.29	0.02	n.d.	n.d.	n.d.	0.02	n.d.	97.47
PFI-39															
8a	53.76	45.45	0.03	n.d.	n.d.	n.d.	n.d.	n.d.	0.01	0.04	n.d.	n.d.	0.03	0.07	99.38
9a	52.54	45.95	0.03	n.d.	n.d.	n.d.	n.d.	n.d.	n.d.	n.d.	n.d.	n.d.	n.d.	0.02	98.54
10a	53.32	46.24	0.08	n.d.	n.d.	n.d.	n.d.	0.16	n.d.	n.d.	n.d.	n.d.	n.d.	0.04	99.85
12a	54.75	46.52	0.04	0.10	n.d.	n.d.	n.d.	0.12	n.d.	n.d.	n.d.	n.d.	0.03	0.05	101.62
19a	52.56	45.37	0.05	n.d.	n.d.	n.d.	n.d.	0.06	n.d.	n.d.	n.d.	n.d.	n.d.	0.04	98.08
24a	54.01	46.63	0.04	n.d.	n.d.	n.d.	n.d.	n.d.	0.01	n.d.	n.d.	n.d.	n.d.	0.04	100.72
26a	54.08	46.17	0.04	n.d.	n.d.	n.d.	n.d.	0.15	n.d.	n.d.	n.d.	n.d.	0.02	0.04	100.49
29a	52.75	45.96	0.05	n.d.	n.d.	0.06	n.d.	1.77	0.02	n.d.	n.d.	n.d.	0.02	0.03	100.65
30a	53.73	46.07	0.10	n.d.	n.d.	0.03	n.d.	0.18	n.d.	n.d.	n.d.	n.d.	0.02	0.04	100.18
31a	54.37	46.80	0.07	n.d.	n.d.	0.02	n.d.	0.04	0.01	n.d.	n.d.	n.d.	n.d.	0.03	101.34
32a(T1)	53.25	46.93	0.06	n.d.	n.d.	0.01	n.d.	n.d.	n.d.	n.d.	n.d.	n.d.	n.d.	0.03	100.27
32a(	53.0	46.59	0.08	n.d.	n.d.	0.03	n.d.	0.22	n.d.	n.d.	n.d.	n.d.	n.d.	0.03	99.99

T1)	3														
32a(T1)	53.73	46.79	0.07	n.d.	n.d.	n.d.	n.d.	n.d.	n.d.	n.d.	n.d.	n.d.	n.d.	0.03	100.62
32a(T1)	54.25	46.87	0.06	n.d.	n.d.	n.d.	n.d.	0.04	n.d.	n.d.	n.d.	n.d.	n.d.	0.03	101.25
32a(T1)	53.63	46.74	0.07	n.d.	n.d.	0.06	n.d.	0.66	0.01	n.d.	n.d.	n.d.	n.d.	0.04	101.20
32a(T1)	53.67	46.71	0.06	n.d.	n.d.	0.02	n.d.	0.05	n.d.	n.d.	n.d.	n.d.	0.02	0.03	100.56
32a(T1)	53.40	46.61	0.07	n.d.	n.d.	0.04	n.d.	0.35	n.d.	n.d.	n.d.	n.d.	n.d.	0.04	100.50
33a	52.52	46.50	0.08	n.d.	n.d.	0.03	n.d.	0.13	n.d.	n.d.	n.d.	n.d.	n.d.	0.04	99.28
34a(T2)	53.18	46.25	0.11	n.d.	n.d.	0.05	n.d.	0.21	n.d.	n.d.	n.d.	n.d.	0.02	0.05	99.88
34a(T2)	53.62	46.67	0.04	n.d.	n.d.	n.d.	n.d.	n.d.	n.d.	n.d.	n.d.	n.d.	n.d.	0.04	100.36
34a(T2)	53.56	46.75	0.04	n.d.	n.d.	n.d.	n.d.	n.d.	n.d.	n.d.	n.d.	n.d.	0.02	0.05	100.42
34a(T2)	53.24	46.39	0.06	n.d.	n.d.	n.d.	n.d.	0.06	n.d.	n.d.	n.d.	n.d.	0.02	0.04	99.81
36a	53.80	46.50	0.04	n.d.	n.d.	0.02	n.d.	0.25	0.01	n.d.	n.d.	n.d.	n.d.	0.04	100.67
39a	53.85	46.41	0.03	n.d.	n.d.	n.d.	n.d.	n.d.	n.d.	n.d.	n.d.	n.d.	n.d.	0.05	100.34
40a	53.80	46.17	0.04	0.01	n.d.	0.01	0.02	0.03	0.01	0.01	n.d.	n.d.	0.03	0.05	100.18

41a	52.64	46.12	0.04	0.02	n.d.	n.d.	0.07	n.d.	n.d.	n.d.	n.d.	n.d.	n.d.	0.04	98.92
42a	53.56	46.15	0.03	n.d.	n.d.	n.d.	n.d.	n.d.	n.d.	n.d.	n.d.	n.d.	0.02	0.04	99.81
44a(T3)	53.51	46.64	0.06	n.d.	n.d.	n.d.	n.d.	n.d.	n.d.	n.d.	n.d.	n.d.	n.d.	0.04	100.25
44a(T3)	53.00	45.89	0.07	1.58	n.d.	0.05	n.d.	n.d.	0.01	n.d.	n.d.	n.d.	n.d.	0.03	100.64
44a(T3)	53.72	46.87	0.07	0.06	n.d.	0.04	n.d.	n.d.	n.d.	n.d.	n.d.	n.d.	0.02	0.04	100.81
44a(T3)	52.95	46.64	0.08	n.d.	n.d.	0.03	n.d.	0.03	n.d.	n.d.	n.d.	n.d.	n.d.	0.02	99.74
44a(T3)	52.80	45.99	0.07	n.d.	n.d.	0.01	n.d.	n.d.	n.d.	n.d.	n.d.	n.d.	n.d.	0.03	98.91
44a(T3)	53.25	46.34	0.05	n.d.	n.d.	n.d.	n.d.	n.d.	n.d.	n.d.	n.d.	n.d.	n.d.	0.04	99.69
45a(T4)	52.84	46.01	0.06	0.02	n.d.	0.02	n.d.	1.19	0.03	n.d.	n.d.	n.d.	0.02	0.04	100.22
45a(T4)	51.77	44.93	0.05	0.05	n.d.	2.04	n.d.	1.17	0.02	n.d.	n.d.	n.d.	n.d.	0.04	100.07
45a(T4)	51.38	45.23	0.04	n.d.	n.d.	1.34	n.d.	1.32	0.02	n.d.	n.d.	n.d.	n.d.	n.d.	99.33
46a(T5)	53.95	46.40	0.05	n.d.	n.d.	n.d.	n.d.	0.39	n.d.	n.d.	n.d.	n.d.	0.02	0.05	100.85
46a(T5)	53.98	46.51	0.04	n.d.	n.d.	n.d.	n.d.	0.36	n.d.	n.d.	n.d.	n.d.	0.02	0.04	100.95

46a(T5)	53.83	46.81	0.04	n.d.	n.d.	n.d.	n.d.	0.26	0.01	n.d.	n.d.	n.d.	0.02	0.04	101.01
46a(T5)	53.32	46.44	0.05	0.04	n.d.	0.02	n.d.	0.22	0.01	n.d.	n.d.	n.d.	n.d.	0.04	100.14
46a(T5)	53.79	46.97	0.11	n.d.	n.d.	0.02	n.d.	0.43	0.01	n.d.	n.d.	n.d.	n.d.	0.04	101.38
46a(T5)	53.33	46.66	0.07	n.d.	n.d.	0.02	n.d.	0.36	0.01	n.d.	n.d.	n.d.	n.d.	0.03	100.47
46a(T5)	53.48	46.75	0.07	n.d.	n.d.	n.d.	n.d.	0.26	0.01	n.d.	n.d.	n.d.	n.d.	0.03	100.60
47a	53.42	45.71	0.14	n.d.	n.d.	n.d.	0.06	0.62	0.03	n.d.	n.d.	n.d.	0.02	0.04	100.04
49a	53.09	46.26	0.19	n.d.	n.d.	n.d.	0.04	0.98	0.01	n.d.	n.d.	n.d.	n.d.	0.03	100.60
50a	52.97	46.82	0.07	n.d.	n.d.	n.d.	n.d.	0.62	0.03	n.d.	n.d.	n.d.	n.d.	0.03	100.53

1123

1124

Table 4.2. *Secondary Ion Mass Spectrometry (SIMS) Analyses of Au, Ag, Co, Cu, As, Sb, Se and Te in Pyrite from the Tolhuaca Geothermal System.*

	Au (ppm)	Ag (ppm)	Co (ppm)	Cu (ppm)	As (ppm)	Sb (ppm)	Se (ppm)	Te (ppm)
PFI-2								
01pyc131	0.40	2.21	10.30	444.00	24.00	n.d.	0.15	n.d.
01pyc133	0.11	3.74	116.00	1123,00[a]	226.00	22.70	0.03	n.d.
01pyc135	0.08	2.26	34.20	277.00	1132.00	36.20	0.03	n.d.
01pyc138	0.03	10.50	274.00	21.30	#######	6.33	0.53	0.10
01pyc139	0.03	4.05	141.00	837.00	384.00	23.50	0.03	n.d.
01pyc140	0.02	2.21	114.00	1091.00	206.00	13.80	0.15	n.d.
01pyc142	0.05	6.33	105.00	553.00	#######	45.30	0.08	n.d.
01pyc144	0.17	6.53	101.00	472.00	#######	16.90	3.43	n.d.
01pyc148	0.02	3.13	223.00	420.00	4535.00	34.00	0.03	n.d.
01pyc150	0.13	10,60[a]	14.60	234.00	#######	35.00	0.95	n.d.
01pyc151	0.16	0.32	13.40	71.40	244.00	4.20	n.d.	n.d.
01pyp129	0.07	1.25	73.30	862.00	839.00	22.40	0.10	n.d.
01pyp130	0.25	4.18	705.00	1425.00	158.00	7.98	0.13	n.d.
01pyp132	0.07	7.20	261.00	1165.00	9887.00	58.40	0.48	n.d.
01pyp134	n.d.	10.40	426.00	5980.00	#######	88.00	0.43	n.d.
01pyp136	0.10	6.98	457.00	3112.00	235.00	12.00	0.18	n.d.
01pyp137	0.06	8.16	1173.00	2950.00	824.00	10.80	0.40	n.d.
01pyp141	n.d.	n.d.	1220.00	2243.00	288.00	n.d.	n.d.	n.d.
01pyp143	0.13	7.77	653.00	2175.00	#######	71.10	0.40	n.d.
01pyp145	0.17	10.70	1544.00	2847.00	4484.00	47.60	1.70	n.d.
01pyp146	0.08	4.72	247.00	1988.00	834.00	25.20	0.13	0.10
01pyp147	0.11	4.96	222.00	1490.00	2248.00	34.70	0.30	n.d.
01pyp149	0.02	4.08	92.40	809.00	2246.00	55.70	0.03	0.28
PFI-3								
01pyc01	0.15	4.60	182.00	274.00	2136.00	24.90	1.33	1.35
01pyc06	3.58	30.90	5.74	3354.00	136.00	68.40	1.20	22.50
01pyc07	n.d.	1.04	243.00	422.00	1193.00	9.90	0.85	0.25
01pyc08	n.d.	1.82	247.00	471.00	2805.00	41.00	0.55	0.10
01pyc15	0.12	3.45	423.00	1124.00	1893.00	54.80	1.18	n.d.
01pyc18	0.06	n.d.	3.39	4.48	12.50	0.00	14.30	0.88
01pyc19	0.01	2.66	239.00	196.00	5355.00	28.90	2,68[a]	0.33
01pyc22	0.11	3.45	117.00	654.00	988.00	57.50	0.43	0.58
01pyc23	0.02	1.44	136.00	323.00	3615.00	22.00	0.63	n.d.
01pyp02	0.15	3.51	900.00	2202.00	2925.00	81.90	2.70	n.d.
01pyp04	0.10	4.84	406.00	1405.00	1505.00	59.40	3.20	0.90
01pyp05	15,40[a]	5.54	5.99	3572.00	158.00	10.20	1.58	13.80
01pyp09	0.24	5.24	1055.00	3928.00	1817.00	94.10	5.93	0.30
01pyp10	0.43	5.66	669.00	1708.00	1963.00	80.90	2.45	0.58

01pyp12	0.26	4.86	823.00	5155.00	1303.00	76.30	3.03	0.13
01pyp13	0.03	1.78	199.00	1335.00	2727.00	74.40	0.88	1.08
01pyp14	0.03	1.51	720.00	1202.00	2907.00	55.80	3.90	n.d.
01pyp16	4,63[a]	1.32	7.85	4962.00	31.70	0.00	1.60	0.60
01pyp17	0.01	3.86	1292.00	3184.00	2440.00	44.60	2.38	n.d.
01pyp20	n.d.	1.52	304.00	461.00	4058.00	57.50	0.13	n.d.
01pyf03	0.28	7.54	120.00	296.00	672.00	40.90	0.75	1.55
01pyf11	n.d.	0.62	142.00	805.00	517.00	20.30	1.98	n.d.
01pyf21	0.19	2.35	147.00	448.00	490.00	29.50	0.83	0.38

1125

1126